Rhythmic coordination of hippocampal-prefrontal ensembles for odor-place associative memory and decision making

Authors: Claire A. Symanski[1+], John H. Bladon[1,2+], Emi T. Kullberg[1,2], Paul Miller[1,3], and Shantanu P. Jadhav[1-4,*]

Affiliations:

[1]Neuroscience Program, Brandeis University, Waltham, MA, 02453, USA

[2]Department of Psychology, Brandeis University, Waltham, MA, 02453, USA

[3]Volen National Center for Complex Systems, Brandeis University, Waltham, MA, 02453, USA

[4]Lead Contact

+ These authors contributed equally to this work

*Correspondence to: shantanu@brandeis.edu (S.P.J.)

ABSTRACT

Memory-guided decision making involves long-range coordination across sensory and cognitive brain networks, with key roles for the hippocampus and prefrontal cortex (PFC). To investigate these coordination mechanisms, we monitored activity in hippocampus (CA1), PFC, and olfactory bulb in rats performing an odor-place associative memory guided decision task on a T-maze. During odor sampling, the beta (20-30 Hz) and respiratory (7-8 Hz) rhythms (RR) were prominent across the three regions, with CA1-PFC beta and RR coherence enhanced during the odor-cued decision making period. Beta phase modulation of CA1 and PFC neuronal activity during this period was linked to accurate decisions, suggesting that this temporal modulation influences sensory-cued decision making. Single neurons and ensembles in both CA1 and PFC encoded and predicted animals' upcoming choices. Our findings indicate that rhythmic coordination within the hippocampal-prefrontal network supports utilization of odor cues for memory-guided decision making.

KEYWORDS

Hippocampus; Prefrontal cortex; Beta oscillations; Respiratory rhythm; Phase locking; Decision making; Olfactory Bulb

INTRODUCTION

The ability to recall associations from memory and use them to guide behavior is a key aspect of cognition across species. Animals can associate sensory cues in the environment with rewarding and noxious experiences and utilize these cues for adaptive behavior. Memory-guided decision making demonstrates the brain's remarkable ability to link familiar cues with actions and beneficial outcomes, but little is known about the mechanisms responsible for this cognitive function.

Neurons that encode learned associations and reflect upcoming choice behavior have been reported in multiple regions in different sensory modalities (Allen et al., 2016; Fitzgerald et al., 2011; Harvey et al., 2012; Igarashi et al., 2014; Johnson and Redish, 2007; McKenzie et al., 2014; Moita et al., 2003; Otto and Eichenbaum, 1992b; Schoenbaum and Eichenbaum, 1995b; Shadlen and Newsome, 2001; Singer et al., 2013; Wirth et al., 2009; Wirth et al., 2003; Yanike et al., 2004). However, sensory cued decision-making based on learned associations necessarily involves a brain-wide network that links primary sensory areas, the medial temporal lobe, and higher cortical areas involved in executive function. Numerous studies have highlighted the significance of the hippocampus and prefrontal cortex (PFC) in cognitive processing related to memory and decision making (Battaglia et al., 2011; Euston et al., 2012; Floresco et al., 1997; Lee and Solivan, 2008; Miller and Cohen, 2001). Both regions are known to encode behaviorally relevant cues and task features (Gothard et al., 1996; Hyman et al., 2012; Wiener et al., 1989; Wirth et al., 2009; Wirth et al., 2003; Yanike et al., 2004), and have been shown to play key roles in memory recall (Fortin et al., 2004; Hasegawa, 2000; Siegle and Wilson, 2014; Wiltgen et al., 2004). Notably, coordinated activity between the hippocampus and PFC, supported by bidirectional anatomical connections (Cenquizca and Swanson, 2007; Delatour and Witter, 2002; Ito et al., 2015), has been shown to be critical for learning and memory-guided behavior (Maharjan et al., 2018; Place et al., 2016; Shin and Jadhav, 2016;

Shin et al., 2019; Yu and Frank, 2015; Zielinski et al., 2020). Therefore, we focused on the coordinated interactions between hippocampus and PFC as a potential key mechanism through which learned associations are recalled and translated into memory-guided decisions.

Several studies have shown that rhythmic network oscillations in the local field potential (LFP) are involved in long-range interactions between the hippocampus and PFC (Benchenane et al., 2011; Buzsaki and Draguhn, 2004; Colgin, 2011; Gordon, 2011; Jones and Wilson, 2005; Shin and Jadhav, 2016). In particular, phase coherence in distinct frequency bands across this network has been suggested as a mechanism for network coordination underlying mnemonic functions. Notably, hippocampal-prefrontal coherence in the theta rhythm (6-12 Hz) and phase-locked spiking plays a role in spatial working memory and acquisition of spatial tasks (Benchenane et al., 2010; Gordon, 2011; Hyman et al., 2010; Jones and Wilson, 2005). However, whether similar mechanisms of coordination between hippocampus and PFC underlie decision making based on sensory cued associations is unclear.

Rodents rely heavily on odor cues for navigation and foraging, so odor memories are highly salient and robust (Abraham et al., 2004; Eichenbaum, 1998; Rinberg et al., 2006; Uchida and Mainen, 2003), making olfactory memory tasks ideally suited for studying memory-guided decision making. Previous studies using odor memory tasks have found prominent beta (20-30 Hz) oscillations in olfactory regions and the medial temporal lobe during cue sampling, suggesting that the beta rhythm acts as a potential mode of long-range communication for olfactory information processing (Frederick et al., 2016; Igarashi et al., 2014; Kay and Beshel, 2010; Rangel et al., 2016; Stopfer et al., 2003). In addition to the beta rhythm, the respiratory rhythm (RR; 7-8 Hz), driven by the animal's breathing cycle, is also prominent in the hippocampus during mnemonic processing of odor stimuli (Karalis and Sirota, 2022; Kay, 2005; Kepecs et al., 2006; Lockmann et al., 2016; Nguyen Chi et al., 2016; Verhagen et al., 2007). However, not much is known about the roles of these rhythms in coordinating activity in the hippocampal-prefrontal network during odor-cued decision making.

To elucidate these mechanisms, we employed an odor-place association task in which rats were required to choose the correct trajectory on a T-maze by recalling and utilizing familiar associations between odor cues and reward locations. While rats were performing the task, we recorded simultaneously from the hippocampus and PFC. Given the involvement of both of these regions in odor-memory tasks (Alvarez et al., 2002; Eichenbaum et al., 1986; Fujisawa et al., 2008; Fujisawa and Buzsaki, 2011; Martin et al., 2007; Otto and Eichenbaum, 1992a; Peters et al., 2013; Place et al., 2016), and the role of hippocampal-prefrontal networks in memory-guided behavior (Churchwell et al., 2010; Fortin et al., 2004; Hasegawa, 2000; Moser and Moser, 1998; Wiltgen et al., 2004; Wiltgen et al., 2010), we hypothesized that rhythmic activity in this network may govern the cellular representation of odor-cued decisions underlying behavioral choices. We also monitored LFP activity in the olfactory bulb (OB) in addition to CA1 and PFC, for robust samplings of previously reported olfactory rhythms such as beta and RR, which have been implicated in cognitive processing of olfactory stimuli (Kay, 2014; Kay et al., 2009). Our results point to a role of beta and RR rhythms in coordinating the olfactory-hippocampal-prefrontal network for utilizing learned odor-place associations to inform decisions, and shed light on the cellular and network mechanisms underlying this process.

RESULTS

Odor-place associative memory and decision-making task

The odor-cued spatial associative memory task required rats to sniff at an odor port where one of two possible odors was presented using a calibrated olfactometer (see **Methods**). The rats were required to choose the correct associated reward arm on the T-maze based on the sampled odor identity, where they would receive a reward of evaporated milk (**Fig. 1a**).

Rats were habituated to the maze and pre-trained on the task before surgical implant of a tetrode microdrive array for recording neural data. Following post-operative recovery and

during electrophysiological recording, animals maintained a high level of performance on the task, indicating accurate decision making based on cued recall of odor-place associations (**Fig. 1b**, *n* = 8 rats, 77.0% ± 1.3%, mean ± s.e.m.). Rats were required to hold their nose in the odor port for a minimum of 0.50 seconds on each trial, but could continue sniffing the odor for any length of time after the minimum threshold was reached. The odor was continuously dispensed for the entire duration of time that the rat held its nose in the odor port and was only turned off once the rat disengaged from the odor-port. The average odor-sampling duration before odor port disengagement and odor offset was 0.82 ± 0.02 seconds (mean ± s.e.m. across sessions), and this duration was similar between correct and incorrect trials (**Fig. 1c**; signed-rank test, *p* = 0.71, distribution for all trials shown in **Supplementary Fig. 1a**). The animals' average velocity during the task showed a decrease in speed from the pre-odor period to the odor sampling period in the odor port, followed by an increase in speed after they left the odor port to run to the reward location (**Supplementary Fig. 1b-c**). We observed rapid movement away from the odor-port after odor-port disengagement (**Supplementary Fig. 1d**). In two animals, a thermocouple was implanted in the nasal cavity to measure the sniff rhythm (see **Methods**). There was a small but significant increase in sniff rate during the odor sampling period (7.1 ± 0.39 Hz, mean ± s.e.m.) compared to time matched pre-odor periods (6.2 ± 0.29 Hz, mean ± s.e.m.) (**Supplementary Fig. 1e**).

Notably, we observed that on a majority of trials (95.4% ± 0.12%), the animals' turn direction away from the odor port matched the direction of the T-maze reward arm that they would ultimately choose on that trial. This behavioral phenomenon was not required for successful performance of the task, and it occurred regardless of whether the trial was correct or incorrect (**Fig. 1d**; binomial tests, correct trials: *p* = 0; incorrect trials: p = 1.4e-108). This observation indicates that the rats recall the odor-place association and choose the reward location for each trial *during* the odor sampling period, before exiting the odor port to run toward

118 the reward. The time of disengagement from the odor port thus provides a trial-by-trial estimate
119 of the moment at which the animal executes the decision. The odor sampling period
120 corresponds to odor-cued recall of the learned association and priming of the subsequent
121 decision to turn toward the reward location, with a behavioral report of the decision occurring at
122 odor port offset. We therefore termed this odor sampling period as "the decision-making period,"
123 since it provides a temporal window between odor onset and odor port exit to investigate
124 mechanisms underlying odor-cued decision making.

125

126 **Beta and RR coherence is elevated during odor sampling and decision making**

127 We therefore focused on the decision-making period and first sought to determine the
128 network dynamics that underlie coordination of brain regions during this period. We used a
129 tetrode microdrive array to record local field potentials (LFPs) and single units from the dorsal
130 CA1 region of the hippocampus, the prelimbic region of the prefrontal cortex (PFC, primarily
131 prelimbic area), and the olfactory bulb (OB, only LFP) in rats as they performed the odor-place
132 association task (see **Methods**; **Supplementary Fig. 2a-b**). The thermocouple signal and LFP
133 traces from CA1, PFC, and OB from an example trial are shown in **Fig. 2a**, along with the same
134 LFP signals filtered in the 20-30 Hz band (additional example shown in **Supplementary Fig.**
135 **2c**).

136 We observed a strong increase in power in the beta band (20-30 Hz) during this
137 decision-making period compared to a time-matched pre-odor period across all three regions
138 (**Fig. 2b,d,** signrank test, CA1 p=2.84e-3, PFC p=1.80e-4, OB p=8.3e-6). Similar increases in
139 beta power during odor discrimination tasks have been reported previously in OB, CA1, and
140 lateral entorhinal cortex (Frederick et al., 2016; Igarashi et al., 2014; Kay and Beshel, 2010;
141 Rangel et al., 2016). The respiratory rhythm (RR, 7-8 Hz) was also prominent in the LFP in all

three regions, but did not change significantly following odor onset (**Fig. 2d**). This rhythm, which corresponds to the respiration rate during odor sampling, has previously been shown to be physiologically and mechanistically distinct from the 6-12 Hz hippocampal theta rhythm (Lockmann et al., 2016; Nguyen Chi et al., 2016), although there is overlap between the two frequency bands. Following odor port disengagement and the initiation of running down the track, we observed a small shift in the dominant LFP frequency from RR to the theta band in CA1 and PFC, reflecting the change in behavioral state (**Supplementary Fig. 2e**).

Odor sampling during the decision-making period thus drives prominent increases in beta rhythm power in OB, CA1 and PFC. During the decision-making period, we also found phase-amplitude coupling between beta and RR rhythms in all three regions, consistent with previous findings (Lockmann et al., 2016) (**Supplemental Fig. 2f),** and suggesting a mechanistic relationship between the two rhythms. Despite this relationship, previous literature shows that the two rhythms are differentially generated and maintained in the olfactory system and hippocampus and appear to serve different functions in olfactory processing (Kay, 2014; Kay et al., 2009; Martin et al., 2006; Neville and Haberly, 2003), indicating that the beta rhythm is not merely a harmonic of RR. Indeed, power increases were seen during the odor sampling period only in the beta band (**Fig. 2d** signed-rank tests, n = 26 sessions, CA1 p=2.84e-3, PFC p=1.80e-4, OB p=8.3e-6) and not in the RR band (**Fig. 2d** signed-rank tests, n = 26 sessions, CA1 [decrease in power] p=3.94e-3, PFC p=0.551, OB p=0.949).

The hippocampal-prefrontal (CA1-PFC) network exhibited prominent and consistent coherence at the beta frequency band during odor sampling, prior to the decision execution at odor-port offset (**Fig. 2c,** similar figures for CA1-OB and PFC-OB in **Supplementary Fig. 3b & c**). This coherence was specific to the odor-sampling period: it significantly increased compared to time-matched pre-odor periods (**Fig 2d** bottom, signed-rank test, CA1-OB p = 5.1e-5, CA1-PFC p = 2.8e-3, PFC-OB p = 3.6e-5), and diminished shortly after the rat exited the odor port,

once the decision had been made (**Fig. 2c**). CA1-PFC coherence in the RR band also increased from the pre-odor to the odor-sampling period (**Fig. 2d,** signed-rank test, CA1-OB p = 6.4e-4, CA1-PFC p = 3.9e-3, PFC-OB p = 2.4e-4). During running, after the decision-making period, the prominent low frequency RR coherence shifted to be slightly higher and centered on the canonical theta band (6-12 Hz), similar to what was observed in the LFP power spectrum (**Supplementary Fig. 3a**). Beta and RR coherence between the CA1-OB and PFC-OB regions also increased during odor sampling periods (**Fig. 2d**), with similar temporal dynamics as CA1-PFC beta coherence.

To control for the possibility that elevated beta coherence during the decision-making period may simply be a reflection of passive movement preparation, as has been observed in sensorimotor cortex (Donoghue et al., 1998), we compared CA1-PFC beta coherence during the last 500 ms of the decision-making period with the 500 ms just prior to reward well exit. We confirmed that beta coherence observed during the decision-making period was significantly higher than coherence at the reward well. **(Supplementary Figure 3f, g,** signed-rank test, CA1-PFC *p* = 0.01, CA1-OB p=0.0012, PFC-OB p=0.0024). Interestingly, this effect in RR was observed for CA1-OB and PFC-OB, but not between CA1-PFC (**Supplementary Figure 3f, g**, signed-rank test CA1-PFC p=0.569, CA1-OB p=0.0044, PFC-OB p=0.00064), suggesting that in contrast to CA1-PFC beta coherence, the increase in CA1-PFC RR coherence was not specific to the decision making period. In an additional control, we also confirmed that this elevated beta coherence was specifically seen during odor-cued decision making and was not present in sessions in which only air was presented at the odor-port, similar to previous reports for beta coherence in CA1-entorhinal cortex (Igarashi et al., 2014) (see **Methods** for description of air-only sessions). In these air-only sessions, reward was given on random trials at the reward locations, even though no odors were presented. RR coherence was unchanged between odor-

191 and air-cued sessions, but beta coherence was significantly lower in the absence of odor cues
192 during air-only sessions (**Supplementary Fig. 3d-e**).

193 We also examined if these beta rhythm dynamics were limited to the odor sampling
194 location on the maze. Indeed, CA1-PFC network beta power and coherence were clearly
195 isolated to the region near the odor port (**Fig. 2f**). Further, since hippocampal sharp-wave
196 ripples (SWRs) have been proposed as a mechanism for memory retrieval, decision making,
197 and planning in some tasks (Carr et al., 2011; Joo and Frank, 2018; Norman et al., 2019; Singer
198 et al., 2013), we investigated the occurrence of SWRs during our task. SWR events occurred
199 frequently at the two reward locations, as expected (Buzsaki et al., 1983). However, a distinct
200 lack of SWR events at the odor port (**Figs. 2f** and **2g**; signed-rank test, p = 1.1e-7) suggests
201 that SWR replay is unlikely to play a direct role in decision making based on recalled associative
202 memories for this well-learned task.

203 CA1-PFC beta coherence was thus specifically enhanced during the odor sampling and
204 decision making period, suggesting that beta rhythms can play a role in odor-cued decision
205 making in this task. The prevalence of RR rhythms also suggests a possible role in organizing
206 sensory information transfer in odor tasks, as suggested by previous studies (Kay, 2005;
207 Kepecs et al., 2006; Nguyen Chi et al., 2016). We, however, did not find a direct relationship
208 between the strength of either beta coherence or RR coherence to correct performance on the
209 task. There was no significant change in the level of coherence or power in the CA1-PFC
210 network in either frequency band between correct and incorrect trials (**Fig. 2e,** signed-rank
211 tests; all p's > 0.05). Therefore, while beta coherence in the CA1-PFC network is elevated
212 during odor-cued decision making, the strength of overall oscillatory coordination in the network,
213 as assessed by coherence, may not directly enable a correct decision, suggesting that
214 oscillatory phase modulation of neuronal activity may instead play a role.

215

216 **Single neurons in CA1 and PFC exhibit choice selectivity during decision-making period**

217 In addition to LFP, we assessed neuronal activity in the task by recording single units
218 from hippocampal area CA1 (n = 1,309 units) and PFC (n = 717 units) (distribution of neurons
219 across animals shown in **Supplementary Table 1**). Units that were active during run sessions
220 were categorized into pyramidal cells and interneurons based on firing rate and spike width (see
221 **Methods,** CA1: 87% pyramidal, 13% interneurons; PFC: 87% pyramidal, 13% interneurons).
222 Pyramidal cells were then further categorized as task-responsive or task-unresponsive based
223 on whether they exhibited significant changes in firing rate during odor sampling (see **Methods**;
224 n = 125 task-responsive CA1 cells, n = 157 task-responsive PFC cells). We observed an overall
225 increase in spiking during the odor sampling period in the task-responsive cell population,
226 suggesting that the majority of these cells increase their firing rate during this period
227 (**Supplementary Fig. 4a**). Interestingly, however, there was an overall decrease in spiking in
228 the average peri-stimulus time histograms when pooling all spikes from all cells during the odor-
229 sampling period (**Supplementary Fig. 4b**). This suggests a decrease in overall activity in CA1
230 and PFC networks during odor sampling, with the task-responsive neurons representing a
231 subset of neurons that were especially engaged in the association and decision-making task.
232 Additionally, we confirmed that task responsive neurons were not simply modulated by the
233 animals' decrease in speed at the odor-port by comparing firing rates during odor sampling to
234 firing rates during reward consumption, when speed was also low. We found task-responsive
235 cells' firing rates were significantly higher at the odor port than at the reward wells
236 (**Supplementary Fig. 4c**).

237 A subset of task-responsive cells was selective for specific choices, based on the
238 identity of the odor and the associated choice. Selectivity was calculated by generating a
239 selectivity index (SI), in which the difference between the average firing rate response to each
240 odor on correct trials was divided by the sum of the two responses, giving a value between -1

241 and 1 (see **Methods**). To determine significance, the SI value for each cell was compared to a
242 distribution of SIs generated by shuffling the odor identities across trials (n = 42 CA1 selective
243 cells, n = 49 PFC selective cells) (**Figs. 3a** and **3b**). Although the number of selective cells that
244 we observed was relatively low, these numbers were consistent with other studies examining
245 single unit responses to odor stimuli in these regions (Otto and Eichenbaum, 1992b;
246 Schoenbaum and Eichenbaum, 1995a; Taxidis et al., 2020).

247 Peri-stimulus time histograms and raster plots aligned to decision time for two example
248 selective cells for CA1 and PFC are shown in **Figs. 3c** and **3g** respectively. Notably, we found
249 that on incorrect trials, selective cells often exhibited responses to the two odors that were
250 opposite to the responses on correct trials (examples shown in **Figs. 3d** and **3h**). We found that
251 this phenomenon held true across the population of selective cells, such that overall, the SIs on
252 correct trials were anti-correlated with the SIs on incorrect trials (**Figs. 3e-f** and **3i-j).** Note that
253 since there are only two possible choices on the task, the behavioral response on an incorrect
254 trial is identical to that of a correct trial of the opposite odor. The fact that the neural responses
255 on trials with identical behavioral responses are similar indicates that selective cells are not
256 simply coding the odor identity but are instead responsive to the animal's memory-guided
257 decision and upcoming behavioral choice. In contrast, selectivity to the odor identity alone would
258 result in similar responses to a given odor regardless of the upcoming behavior or the ultimate
259 trial outcome. We therefore termed these cells choice-selective cells. This pattern was not
260 significant within the population of neurons that were task-responsive but did not meet the
261 selectivity threshold (**Supplementary Fig. 4d-e**). Histograms showing distribution of absolute
262 selectivity indices between selective and nonselective cells are shown in **Supplementary 4f.**

263 Putative interneurons were also divided into task-responsive and task-unresponsive,
264 using the same criteria as for putative pyramidal cells (**Fig. 4a**). **Fig. 4b-c** shows interneuron
265 odor selectivity indices and response properties during correct and incorrect trials. For CA1

interneurons, the selectivity response showed anti-correlation during correct versus incorrect trials similar to that of pyramidal cells. PFC interneurons' SIs on correct and incorrect trials were not anti-correlated, although this could result from the low number of selective PFC interneurons overall.

To investigate whether there was evidence of coordination between ensembles in CA1 and PFC, we wanted to determine whether the spiking of neuronal ensembles in the two regions were temporally linked (Jadhav et al., 2016; Siapas et al., 2005). In order to examine this, we computed the normalized spiking cross-correlation for all CA1-PFC pairs of task-responsive neurons during odor sampling (**Fig. 4d, Methods**). Significant peak time lags of cross-correlations were quantified for all CA1-PFC task-responsive putative pyramidal cells (n = 224 pairs), all pairs of task-responsive interneurons (n = 87 pairs), as well as pairs of CA1 interneurons and PFC pyramidal cells (n = 298 pairs), and vice versa (n = 113 pairs). We found a significant skew in CA1-PFC interneuron pairs towards the PFC interneurons leading (sign rank test, x=-.028, p=3.5e-8) (**Fig. 4d**), as well as for CA1 pyramidal cell - PFC interneuron pairs in the same direction (sign rank test, x=-.013, p=0.0034). Additionally, we found a large cluster of CA1 interneuron- PFC pyramidal cell pairs whose cross-correlations peaked around -.035 sec and one at +.01 sec, or approximately the period of a beta cycle.

These results further illustrate temporal relationships during the decision making period, and especially suggest that CA1 interneurons show temporal coordination with PFC task-responsive ensembles in the beta range. The strong skew towards PFC interneuron's leading CA1 interneurons and CA1 pyramidal cells suggest top down influence of the PFC on CA1 just before the animal begins to execute its decision. Since interneurons have a pre-dominant effect on local network activity, common input to the CA1-PFC network, especially to interneurons, can potentially play a key role in temporally organizing ensemble responses in both regions

290 (Andrianova et al., 2021; Dolleman-van der Weel et al., 2019; Schlecht et al., 2022; Varela et
291 al., 2014).

292

293 **CA1 and PFC cells phase lock to beta and respiratory rhythms during decision making**

294 We next asked if there was any relationship between oscillatory phase modulation of
295 neuronal activity and decision accuracy. A subset of cells within the population of task-
296 responsive cells in both CA1 and PFC were phase locked to the beta rhythm during the
297 decision-making period (see **Methods**; CA1: pyr n = 12/86, 14.0%, int n = 29/71, 40.9%; PFC:
298 pyr n = 6/92, 6.5%, int n = 4/33, 12.1%), and many cells in the task-responsive populations were
299 also strongly phase locked to RR (CA1: pyr n = 59/86, 68.6%, int n = 66/71, 92.9%; PFC: pyr n
300 = 15/92, 16.3%, int n = 10/33, 30.3%). Spike-phase histograms for example beta-phase and
301 RR-phase locked cells in CA1 and PFC are shown in **Fig. 5a & Fig 5b** (Rayleigh Z test, CA1: n
302 = 242 spikes, z = 15.4, p = 1.5e-7; PFC: n = 99 spikes, z = 40.9%, p = 0.007), and the
303 preference for all coherent cells is shown in polar plots (**Fig. 5c & d**). Interestingly, even though
304 a higher percentage of cells in both regions were phase locked to RR (**Fig. 5e**, z-test for
305 proportions, CA1: p = 6.8e-23; PFC: p = 8.8e-9) and depth of this modulation was much
306 stronger for RR compared to beta (**Supplementary Fig. 5a**), phase preference across cells was
307 consistent only in CA1, but for both rhythms (**Fig 5c, d,** Rayleigh Z-test, CA1: n=157 beta
308 p=4.3e-6, RR p=2.01e-5; PFC n=125, beta p=0.70, RR p=0.13). Additionally, in both CA1 and
309 PFC, the proportion of cells that were phase locked to both beta *and* RR was no different than
310 chance, given the percentages of cells that were modulated by either rhythm (**Supplementary**
311 **Fig. 5b**). This suggests that the two rhythms simultaneously modulate different populations of
312 cells, supporting the interpretation that the two rhythms play separate, though cooperative, roles
313 in memory-guided decision making.

Are cells that are modulated by beta the same population of cells that are selective for the upcoming decision? To test this, we compared the number of pyramidal cells that were both choice-selective *and* phase-locked (within and across regions) to the fraction that would be expected by chance, given the total percentages of cells that are choice-selective or phase-locked. Interestingly, we found that the number of cells that met both criteria was no different than chance for either CA1 or PFC (**Supplementary Fig. 5c**, binomial tests; CA1: p = 0.097; PFC: p = 0.17). We found similar results for interneurons in each region, as well as for RR modulation (**Supplementary Fig. 5d, e**). It should be noted that since such a large majority of neurons in CA1 were significantly phase locked to RR, it is unsurprising that almost all the choice-selective cells were phase locked to this rhythm. However, this result indicates that the choice-selective cells were no more or less likely than non-selective cells to phase lock to RR as well. These results together suggest that the putative neural ensembles that are selective for the primary task parameter of odor-cued associative decisions may not be driven directly by the beta rhythm via prevalence of phase-locking.

We next asked whether the strength of phase locking to the rhythms was still indicative of decision accuracy by comparing correct versus incorrect trials. To do this, we compared each cells mean vector length (MVL) after adjusting for rate differences (Rangel et al., 2016), a measure of non-uniformity in the spike-phase distribution, on correct versus incorrect trials for all task responsive cells. For each cell, we calculated the MVL for the spike-phase distribution on correct trials and incorrect trials separately and compared these two paired distributions. We found interneurons in both CA1 and PFC as well as pyramidal cells in CA1 that were phase-locked to the local beta rhythm exhibited a lower MVL on incorrect trials (**Fig. 5f**, signed-rank tests, CA1: pyr n = 90, p = 0.019, in n=73, =p2.61e-3; PFC: pyr n = 98, p = 0.25, in n=33, p=0.043). There was no significant effect for the RR phase locking (**Fig 5h,** signed-rank test, no significance found), and neither was there for cross-regional beta modulation (**Supplemental**

339 **Fig 5f**). This suggests that local spiking modulation by the beta rhythm in CA1 and PFC can
340 potentially play a role in supporting accurate utilization of odor-place associations for making
341 decisions. Together with the observed temporal coordination between task-responsive
342 interneurons across regions (**Fig. 4d**), these data suggest that rhythmic coordination between
343 PFC and CA1 via the beta rhythm supports successful memory guided behavior in this
344 paradigm.

345 The stronger local beta phase modulation in CA1 during correct trials and elevated CA1-
346 PFC beta coherence during decision making periods (**Fig. 2d**) together suggests that beta
347 coordination is related to task performance. The higher beta phase modulation of CA1 and PFC
348 interneurons also suggests that entrainment of interneurons to the network-wide beta rhythm is
349 linked to task performance as well. This also aligns with the finding of temporal relationships in
350 cross-correlations between PFC interneurons and CA1 pyramidal cells and interneurons (**Fig.**
351 **4d**). Rhythmic modulation of interneurons, possibly through a common input, can potentially
352 constrain and coordinate network activity, and may play a role in sculpting pyramidal cell
353 ensembles in local circuits to enable processing of odor-cued associations for translation to
354 decisions.

355

356 **Neural ensemble responses in CA1 and PFC during decision making predict the**
357 **upcoming choice**

358 Given the choice-selective responses of single neurons in CA1 and PFC (**Figs. 3-4**), and
359 the relationship of phase modulation to decision accuracy (**Fig. 5**), we next examined how
360 ensemble dynamics underlie the neural representation of decisions informed by odor-cued
361 recall. We considered all cells that were task-responsive, including putative pyramidal cells and
362 interneurons, for the ensemble analyses. For the population of task-responsive cells, we found

363 that the distribution of the peak response times in both CA1 and PFC tiled the entire decision
364 time window (**Fig. 6a**).

365 We then examined the temporal evolution of CA1 and PFC ensemble responses in
366 individual sessions to infer the timing of neural discrimination. Principal component analysis
367 (PCA) was applied to visualize the temporal dynamics of population activity during the decision
368 making period, and the Euclidean distance between left-bound and right-bound neural
369 trajectories was used as a measure of neural discrimination (see **Methods**). **Figure 6b** shows
370 an example session with average trajectories of CA1 population activity using the first three PC
371 dimensions for the two choices (n = 12 CA1 neurons in ensemble, 100 ms bins; n = 43 left-
372 bound and n = 45 right-bound trials). The two trajectories show a rapid evolution and
373 separation within a few hundred milliseconds after odor onset. The Euclidean distance between
374 left-bound and right-bound average trajectories was compared to a chance-level distance
375 distribution computed by shuffling the trial identities across trials and creating a null distribution.
376 The timepoint at which the population responses were considered significantly distinct from
377 each other was defined as the first bin at which the real distance between trajectories surpassed
378 the 95% confidence interval of the null (shuffled) distribution (shown in **Fig. 6c** for one example
379 session for CA1 and PFC each. Neural discrimination times for CA1 and PFC (n = 24 sessions
380 across 8 animals; threshold of 4 task-responsive cells, CA1 mean: 200-800 ms; PFC mean:
381 400-700 ms) were similar (**Fig. 6d**; p = 0.68, sign-rank test).

382 To determine whether the animal's upcoming behavior could indeed be predicted by
383 neural ensembles before the decision was executed, we trained a generalized linear model
384 (GLM) to predict the animal's choice based on ensemble activity during the decision-making
385 period (See **Methods**). We performed this analysis using task-responsive putative pyramidal
386 cells and found that reward choice could be accurately predicted 0.1 seconds prior to odor port
387 disengagement by CA1 ensembles, and 0.3 seconds prior by PFC ensembles (**Fig. 6e**).

388 Additionally, we performed the same analysis, but included both task-responsive pyramidal and
389 interneurons in the ensembles. In this case, we found an improvement in prediction for CA1
390 ensembles: reward prediction was now accurate starting earlier, at 0.2 seconds prior to decision
391 execution. Prediction by PFC ensembles remained the same. (**Fig. 6e**). To control for the
392 possibility that inclusion of interneurons improved prediction latency for CA1 simply due to the
393 larger number of cells in the training set, we performed this analysis again by resampling the
394 pyramidal cells to match the total number of pyramidal cells plus interneurons**.** In this control
395 analysis, we found that the choice could again only be predicted at 0.1 seconds prior to the
396 decision execution, the same as what we observed with the original sample of pyramidal cells.
397 These results confirm that the animals utilize the recalled odor-place association and make a
398 spatial choice during this odor-sampling period, which is reflected in the activity of task-
399 responsive neural ensembles.

400

401 **Representations of choice and space are maintained independently during delay period**

402 Finally, we investigated whether there was any relationship between the activity of CA1
403 and PFC ensembles during the odor-cued decision-making period and their spatial activity on
404 the maze as the animals ran through the delay period on the central and side arms toward
405 reward. We examined units from sessions in which animals traversed a long T-maze track (see
406 **Methods**, 26 sessions from 6 rats) in order to assess spatial firing characteristics. A large
407 fraction of cells in CA1 and PFC exhibited spatial activity on the maze (see **Methods** for details
408 on spatial parameters, n = 344 out of 585 CA1 cells; n = 159 out of 288 PFC cells had fields on
409 the track), including units that were both task-responsive (choice selective and non-selective)
410 and task-unresponsive (**Figs. 7a, 7b**; examples of CA1 and PFC choice-selective cells with

411 spatial fields in **Fig. 7a,** examples of CA1 and PFC task-responsive but non-selective cells with
412 spatial fields shown in **Supplementary Fig. 6a**).

413 Cells that were task-responsive were more likely to have spatial fields on the track (odor
414 sampling periods were excluded in spatial responses, see **Methods**), compared to cells that
415 were not responsive during the odor sampling period (**Fig. 7b**, binomial test, CA1: p=0.029;
416 PFC: p=2.7e-5). Additionally, for both CA1 and PFC neurons, we found that the firing rate
417 during odor sampling was correlated with firing rate during running (**Fig. 7c,** CA1: r = 0.39, p =
418 3.0e-37; PFC: r = 0.68, p = 1.2e-62), and task-responsive cells had higher firing rates overall
419 (**Supplementary Fig. 6b**), suggesting a possible relationship between cell activity during
420 decision making and maintenance of the decision during the spatial delay. To examine this
421 question further, we asked whether the spatial fields in either CA1 or PFC exhibited different
422 characteristics based on whether they were responsive during the decision-making period.
423 Surprisingly however, we found no difference in field width (**Fig. 7d,** rank-sum tests, CA1: p =
424 0.15; PFC: p = 0.92), field peak rate (**Supplementary Fig. 6c**), or field sparsity
425 (**Supplementary Fig. 6d**) between cells that were task-responsive and task-unresponsive in
426 either region.

427 Further, we also examined trajectory selectivity as animals ran through the central arm
428 and on the side arms toward reward (examples of trajectory selective firing shown in **Fig. 7a,**
429 second row). Trajectory selectivity was defined by comparing spatial tuning curves of cells on
430 right versus left trajectories and calculating a selectivity index analogous to the choice selectivity
431 index during the decision-making period (see **Methods**). Interestingly, although trajectory-
432 selective cells were significantly more likely than trajectory-nonselective cells to respond in the
433 decision-making period (**Supplementary Fig. 6e**), there was no relationship between the
434 preferred trajectory during run periods and preferred choice during the odor-cued decision-
435 making period (**Fig. 7e,** rank sum test CA1: p = 0.26; PFC: p = 0.20)**.** Thus, although CA1 and

436 PFC cells that were task responsive had higher firing rates and therefore higher engagement
437 while traversing trajectories on the maze, there was no clear relationship between choice
438 selectivity and trajectory selectivity in either CA1 or PFC.

439 To confirm this result, we sought to determine whether choice selective neuronal activity
440 in the population during decision making persisted into the following run period. To examine
441 this, the linearized T-maze was divided into 5 equally spaced quintiles and a Bayesian Classifier
442 trained on odor period activity was used to decode the choice identity from the ensemble activity
443 during run at each spatial quintile (see **Methods**; similar results were seen for spatial quartiles).
444 We found that choice identity could be decoded at the first quintile of track, nearest to the odor
445 port, but decoding accuracy diminished to chance level thereafter (**Fig. 7g**). In contrast, the
446 animal's upcoming behavioral choice could be accurately decoded at all periods along the
447 trajectory if instead the spatially active ensembles in each respective spatial quintile was used
448 as the training set (**Fig. 7h**). This suggests that the choice selectivity that emerges in ensembles
449 during odor sampling (**Fig. 6**) persists transiently for a short period past the decision point, but
450 that separate ensembles maintain choice-related information as animals traverse the spatial
451 trajectory, possibly corresponding to theta oscillations during run (**Supplementary 2g**). This is
452 further supported by the fact that, at least for CA1, choice-selective ensemble firing rate is
453 highest within 20 cm of the odor port, and decreases thereafter (**Supplementary Fig. 6f**).These
454 results together suggest that the choice-selective ensembles reflecting decision making during
455 the odor-cue period transiently encode the choice during the initial track period, but the decision
456 is subsequently maintained by a distinct ensemble during the working-memory period
457 associated with the spatial delay on the central arm.

458

459 **DISCUSSION**

460 These results provide new insight into the mechanisms of rhythmic coordination of
461 hippocampal–prefrontal ensembles by beta rhythms for odor-cued associations and decision
462 making. We found that during an odor-place associative memory task, beta and RR rhythms
463 govern physiological coordination between the olfactory bulb, hippocampus, and PFC. Crucially,
464 CA1-PFC beta coordination was uniquely elevated specifically during the decision-making
465 portion of this task. During the odor sampling and decision-making period, task-responsive
466 single unit and ensemble activity in the CA1-PFC network discriminates between choices and
467 can reliably predict upcoming behavior. CA1-PFC beta coherence was elevated during the
468 decision-making period, but we did not find evidence for difference in coherence for correct vs.
469 incorrect trials. Instead, we found that phase-modulation of cells by beta rhythms was stronger
470 on correct vs. incorrect trials, and in particular, CA1 pyramidal cells, as well as interneurons in
471 both PFC and CA1 exhibited stronger phase modulation by these rhythms during accurate
472 memory-guided decision making. This suggests that coordination by odor-driven beta rhythms
473 may sculpt network activity through interneuron modulation, enabling emergence of task-related
474 ensemble dynamics in local circuits to support decision making. Our results thus suggest that
475 oscillatory modulation plays a key role in temporal evolution of ensemble dynamics in the CA1-
476 PFC network for odor-cued decision making.

477 The mechanisms underlying encoding and recall of associations between sensory cues in
478 the environment, and subsequent use of these associations to guide decisions, are of
479 fundamental interest. Sensory cue-elicited recall and decision making during goal-directed
480 behavior involves widespread networks encompassing sensory regions, medial temporal
481 memory regions, and prefrontal executive function regions. Prominent odor-driven oscillations
482 have been described in these areas (Frederick et al., 2016; Igarashi et al., 2014; Kay and
483 Beshel, 2010; Kepecs et al., 2006; Lockmann et al., 2016; Nguyen Chi et al., 2016; Rangel et
484 al., 2016; Stopfer et al., 2003; Tort et al., 2009), which can potentially coordinate these long-

range networks to enable utilization of familiar olfactory cues to guide behavior. Here, the use of an odor-cued T-maze task allowed us to examine which rhythms enable coordination of olfactory-hippocampal-prefrontal networks, and whether these rhythms play a role in patterning ensemble activity in hippocampal-prefrontal network to enable memory-guided decision making.

In this task, the time period between odor onset and odor port disengagement provided a temporal window corresponding to odor-cued recall and priming of the subsequent decision to turn toward the reward location. We found prevalence of both beta (~20-30 Hz) and RR (~7-8 Hz) across the olfactory-hippocampal-prefrontal network during this odor sampling and decision-making period. The strength of beta coherence between the hippocampus and PFC was enhanced during the decision-making period compared to pre-odor periods as well as period of immobility during reward consumption. Further, while CA1-PFC RR coherence remained unchanged between odor-cued trials and trials where only air was presented, high beta coherence was specific to odor-cued trials corresponding to a decision-making task and was lower on air-cued trials corresponding to random choices. Based on these findings, we speculate that encountering a familiar odor stimulus and efficiently utilizing this associative memory for a decision, rather than respiration or movement preparation (Hermer-Vazquez et al., 2007), elicits the engagement of the hippocampal-prefrontal network by the beta rhythm.

Interestingly, although hippocampal SWRs have been linked to internal recall and planning (Buzsáki, 2015; Carr et al., 2011; Joo and Frank, 2018), there was very low prevalence of hippocampal SWRs during odor sampling, suggesting SWRs are not directly involved in odor-cued associative memory and decision making while the animal is re-encountering the familiar cue. Instead, our results indicate that beta rhythms play a key role in mediating this process, in addition to coordinating entorhinal-hippocampal networks for odor-cued recall, as described previously (Igarashi et al., 2014). In our experiments, rats were very familiar with the task and odor-place associations, with high performance levels. Therefore, the lack of SWRs during the

510 decision-making period could reflect that these memories had been previously consolidated into
511 neocortex during learning, resulting in a shift from largely hippocampal-dependent processing
512 (Igarashi et al., 2014) to processing that is more reliant on hippocampal-cortical dialogue via the
513 beta rhythm.

514 Odor-driven gamma rhythms at 40-100 Hz have also been reported in odor-memory tasks
515 (Beshel et al., 2007; Frederick et al., 2016; Kay, 2014), and may play a complementary role with
516 beta oscillations. It has been hypothesized that local olfactory networks may be governed by
517 gamma rhythms for odor processing early in stimulus sampling, before shifting to a beta-
518 dominant network state as downstream regions are engaged (Frederick et al., 2016; Martin et
519 al., 2006). Our results corroborate this hypothesis by reinforcing the role of the beta rhythm in
520 long-range coordination with a wider network outside the olfactory system for cognitive
521 processing of odor stimuli. We speculate that sensory modality-specific rhythms may play a
522 general role in cue-driven mnemonic decision making by coordinating sensory and cognitive
523 areas, which can be tested in future studies.

524 Our analysis of single units in the hippocampus and prefrontal cortex revealed a group of
525 cells that were selectively responsive in the odor task period, similar to previous reports in the
526 hippocampus (Eichenbaum et al., 1987; Igarashi et al., 2014; Terada et al., 2017). However, we
527 found that these selective cells often exhibited “opposite” selectivity on incorrect trials compared
528 to correct trials, indicating that these cells do not respond solely to the perceptual qualities of the
529 odor, in which case the response would be similar on all presentations of a particular odor
530 regardless of the trial outcome. Instead, this response suggests coding of the behavioral choice
531 associated with the odor cue, resembling findings from studies of combined cue modalities and
532 cue-context associations (Allen et al., 2016; Ferbinteanu et al., 2011; Fitzgerald et al., 2011;
533 Komorowski et al., 2009; McKenzie et al., 2014; Otto and Eichenbaum, 1992b; Schoenbaum
534 and Eichenbaum, 1995b; Terada et al., 2017). Thus, the CA1-PFC neural response during odor

535 sampling corresponds to the decision in response to the odor-place association. Future studies
536 that combine recording from other olfactory regions, such as piriform cortex, together with
537 hippocampus and PFC can potentially unveil how the cue representation evolves from odor
538 perception to the recall-based decision.

539 Task-responsive neural populations exhibited differential activity patterns in response to the
540 two odor-associations during decision making, and the animal's upcoming choice could be
541 predicted from this ensemble activity. Overall, the timing of ensemble odor discrimination
542 preceded choice execution, indicating that the emergence of the neuronal representation can
543 prime the cognitive decision. This emergence of neural ensembles that reflect associative
544 memories governing decision making may also be indicative of a physiological mechanism for
545 dynamic reactivation of memory engrams upon re-encountering the familiar odor stimuli
546 (DeNardo et al., 2019; Liu et al., 2012). It remains unclear, however, how these neural dynamics
547 are modulated by beta oscillations and how they evolve as animals learn new associations. One
548 possibility is that they resemble the dynamics observed in the hippocampal-entorhinal circuit, in
549 which coordination of the network at the beta rhythm and choice-selective neural activity
550 emerge gradually as animals learn the task (Igarashi et al., 2014).

551 Similarly, CA1-OB beta coherence is strong during odor memory tasks and is known to
552 increase over the course of learning (Martin et al., 2007). Although CA1-OB beta coherence
553 was high during odor sampling in our task, we observed no significant relationship between
554 CA1-OB coherence and task performance. Since previous reports suggest that this coherence
555 is linked to the learning process, it is possible that a more direct relationship between coherence
556 strength and performance would be observed only during learning, but not in this case where
557 the odor association and task are familiar. Choice-coding ensemble dynamics may evolve in
558 parallel with the increase in CA1-OB beta coherence over learning, similar to what has been
559 reported in the hippocampal-entorhinal circuit (Igarashi et al., 2014). This possibility can be

560 investigated by examining network dynamics and ensemble activity across multiple olfactory
561 and cognitive areas during novel odor-place learning or reversal learning.

562 It is also noteworthy that we observed different mechanisms underlying odor-cued decision
563 making versus subsequent maintenance of the representation of the choice during a spatial
564 delay period. Odor-driven beta coherence and phase modulation has a role in accurate
565 decisions, and possibly leads to emergence of ensemble selectivity which is predictive of the
566 animal's upcoming choices. However, these ensembles maintain their choice-selectivity only
567 transiently after the decision execution as animals embark on the spatial trajectory toward
568 reward. This selective coding is not maintained by the same ensembles during running, but
569 instead other spatially modulated cells in CA1 and PFC maintain choice coding on the track,
570 including the spatial delay period (common central arm on the T-maze) activity. Thus, beta
571 driven ensembles mediate memory-guided decision making in the hippocampal-prefrontal
572 network, but choice selective activity is then subsequently maintained by theta-driven spatially
573 modulated activity, similar to reports in spatial working memory tasks (Taxidis et al., 2020).

574 The temporal evolution of ensemble activity underlying odor-cued decision making is
575 reminiscent of temporal coding of odor stimuli mediated by oscillations in the olfactory system
576 (Kepecs et al., 2006; Stopfer et al., 2003). Previous findings indicate that spike timing
577 modulation according to the phase of prominent network rhythms can organize task-encoding
578 neural ensembles to support memory guided behavior and decision-making (Benchenane et al.,
579 2010; Buschman et al., 2012; Papale et al., 2016; Terada et al., 2017; Wikenheiser and Redish,
580 2015; Zielinski et al., 2019). Interestingly however, we found that although the strength of local
581 beta phase-modulation was linked to correct decisions, putative neurons that encoded the
582 choice were no more likely to be phase-locked than chance level. Further, we found evidence
583 that different populations of cells are modulated by the two ongoing rhythms during decision
584 making, implying that beta and RR represent two simultaneous modes of rhythmic coordination

585 in the network (Rangel et al., 2016). This joint modulation of the underlying cell populations,
586 along with our finding of strong cross-frequency coupling between the two rhythms, leads us to
587 the interpretation that beta and RR coordinate the network cooperatively during odor-cued
588 decision making. Previous reports of RR in olfactory processing (Karalis and Sirota, 2022; Kay,
589 2005; Kepecs et al., 2006; Nguyen Chi et al., 2016), along with evidence that multiple rhythms
590 can simultaneously modulate ongoing processes (Lisman and Jensen, 2013; Rangel et al.,
591 2016; Zhong et al., 2017), suggests that RR could be the dominant modulator coordinating the
592 sensory element of the task, while beta coordination is key for employing the sensory cued
593 association to make a decision. This interpretation is further supported by our results from un-
594 cued air sessions, which did not involve memory-guided behavior, in which we found a
595 reduction in beta coherence in the network but no change in RR coherence. This suggests that
596 the sensory component of this process is maintained as the animal continues sniffing even in
597 the absence of an explicit cue, whereas beta coordination is only engaged when a familiar cue
598 is utilized for a decision.

599 We also found that a large population of interneurons were strongly modulated by the beta
600 rhythm locally and the further that strength of this modulation was linked to task performance.
601 PFC interneurons also showed temporal coordination with CA1 interneurons and pyramidal
602 cells. This suggests that the beta rhythm can function by modulating interneuron activity, which
603 sculpts ensemble dynamics in the local circuits governing decision making. In this manner, beta
604 oscillations may play a role in establishing communication and organization of activity in sensory
605 and cognitive networks enabling decisions based on cued associations. Thus, oscillatory phase-
606 modulation may be indicative of a general network state that enables coordination.

607 **METHODS**

608 All experimental procedures were approved by the Brandeis University Institutional
609 Animal Care and Usage Committee (IACUC) and conformed to US National Institutes of Health
610 guidelines. Eight male Long-Evans rats (3-6 months, 450-650 g) were used for experiments.
611 Animals were housed individually in a dedicated climate-controlled animal facility on a 12-hour
612 light/dark cycle. All experiments were carried out during light cycle. Upon arrival, animals were
613 provided ad libitum access to food and water and handled regularly to habituate them to human
614 contact.

615

616 **Behavior Apparatus**

617 An olfactometer (MedAssociates Inc.) was used for dispensing odors. The olfactometer
618 continuously dispensed clean air to the odor port until receiving a signal to open a solenoid
619 valve which caused air to flow through liquid odorants, resulting in odorized air dispensed to the
620 odor port. A vacuum tube attached to the odor port was used to continuously collect any
621 residual odorized air between trials. Infrared beams were used at the odor port and reward wells
622 to determine the precise timing of entry and exit from these areas.

623

624 **Odor-Place Association Task Training**

625 Once rats reached a minimum threshold weight of 450 g, they were food restricted to no
626 less than 85% of their free-feeding baseline weight. For initial behavioral training, rats were
627 familiarized with the behavior room, the sleep box, running on a raised track to receive
628 evaporated milk reward, and sniffing odors presented in the odor port. Following this
629 habituation, rats were trained to hold their nose in the odor port for a minimum of 500 ms, with

630 an auditory tone indicating when this 500-ms time threshold was reached. However, the rats
631 could continue to sniff the odor for any longer duration of time, and odor would be continuously
632 dispensed until they disengaged from the odor port. Throughout all training and experiments, if
633 the rat exited the odor port before this threshold was reached, no reward was dispensed
634 regardless of the rat's choice and the rat was required to re-initiate the trial. These prematurely
635 terminated trials were excluded from all analyses. For each trial, the odor sampling period was
636 defined as the time from the onset when rat's nose broke the infrared beam to offset when the
637 beam break was terminated, and odor stimulus was stopped.

638 Animals were subsequently trained on the olfactory association. On each trial, one of
639 two possible odors was dispensed at the odor port in a pseudo-random order. Odor 1 (Heptanol
640 – pine/citrus scent) indicated that the rat should go to Reward 1 to receive reward. Odor 2 (ethyl
641 butyrate – strawberry scent) indicated that the rat should choose Reward 2 (**Fig. 1a**). If the rat
642 ultimately made the correct choice, evaporated milk reward would be dispensed at the chosen
643 reward port upon triggering the infrared beam, whereas upon an incorrect choice no reward was
644 dispensed.

645 Associative memory training was shaped in steps. The rats first learned the association
646 between the odors and "right" vs "left" reward locations with reward wells close to the odor port.
647 On subsequent training days, the reward wells were moved further and further away from the
648 odor port, until rats could comfortably perform the task on the full T-maze (81 cm long center
649 stem, and 43cm long reward arms). Two rats were not trained to run on the full T-maze, and
650 instead were just required to perform the association with the reward wells within easy reach on
651 either side of the odor port. For one animal, the maze had a shortened stem (40 cm instead of
652 81 cm), but the reward wells were still at the ends of the T arms. Task performance was
653 calculated as the proportion of correct trials. Rats were trained until they could perform the task
654 with at least 80% accuracy for 3 consecutive days.

655 Once training was complete, animals were once again provided with *ad libitum* access to
656 food until they reached at least 600 g, before undergoing surgery. After surgery but before
657 recording, rats were briefly re-trained on the association until they could again perform the task
658 with at least 80% accuracy. On recording days, animals were allowed to continue performing
659 the task until they reached satiation, about 100-150 trials per day. Task epochs were interleaved
660 by sleep epochs, in which rats spent about 20 minutes in an opaque sleep box, with a sleep
661 epoch as the first and last epoch of each day.

662

663 **Un-Cued Air Sessions**

664 Four of the animals were tested on one session each in which only clean air was
665 dispensed at the odor port, instead of two distinct odors. Reward was available at a randomly
666 chosen reward port on each trial; although, since the trials were un-cued, the animals would
667 often randomly choose the "incorrect" side and no reward was dispensed (**Supplementary**
668 **Figure 3f**). All other aspects of the task were the same as the odor-cued task.

669

670 **Surgical Procedures**

671 Surgical implantation techniques were performed as described previously (Shin et al.,
672 2019; Tang et al., 2017; Tang et al., 2021). Animals were implanted with a microdrive array
673 containing 30 independently moveable tetrodes targeting right dorsal hippocampal region CA1 (-
674 3.6 mm AP and +2.2 mm ML, 10-12 tetrodes), right PFC (+3.0 mm AP and +0.7 mm ML10-13
675 tetrodes), and right olfactory bulb (+7.2 mm AP and +0.8 mm ML, 1-4 tetrodes). Post-operative
676 analgesic care was provided for 48 hours after surgery to minimize pain and discomfort. In two
677 of the eight animals used for experiments, a nasal thermocouple was implanted in addition to
678 the microdrive array to record the respiratory rhythm. The thermocouple was placed in the left

679 nostril though a hole drilled in the skull at +7.5 mm anterior to the cribriform suture. The
680 thermocouple wire was secured using dental acrylic and soldered to the same printed circuit
681 board as the tetrodes.

682

683 **Tetrode Recordings**

684 For 1-2 weeks following surgery, tetrodes were gradually lowered to the desired depths.
685 Hippocampal tetrodes were targeted to the pyramidal layer of CA1 using characteristic EEG
686 patterns (sharp wave polarity, theta modulation) and neural firing patterns as previously
687 described (Jadhav et al., 2012; Jadhav et al., 2016). The final placement of tetrodes was
688 confirmed in histological preparations using Nissl staining post-mortem. One tetrode in corpus
689 callosum served as hippocampal reference, and another tetrode in overlying cortical regions
690 with no spiking signal served as PFC reference. A ground screw (GND) installed in the skull
691 overlying cerebellum also served as a reference, and LFP was recorded relative to this GND. All
692 spiking activity was recorded relative to the local reference tetrode. Only LFP activity was
693 recorded from the olfactory bulb. Electrodes were not moved at least 4 hours before and during
694 the recording day to reduce drift, and were micro-adjusted at the end of each recording day to
695 sample new cell populations.

696 Data were collected using a SpikeGadgets data acquisition system and software
697 (SpikeGadgets LLC). Spike data were sampled at 30 kHz and bandpass filtered between 600
698 Hz and 6 kHz. LFP signals were sampled at 1.5 kHz and bandpass filtered between 0.5 Hz and
699 400 Hz. The animal's position and running speed were recorded with an overhead color CCD
700 camera (30 fps) and tracked by color LEDs affixed to the headstage.

701

Data Analysis and Statistics

All data analysis was performed in MATLAB using custom code unless otherwise noted. Error bars indicate standard deviation unless otherwise noted. Significance was defined using an alpha of 0.05. Statistical details including tests used, p-values, and n values can be found in figure legends, and are described in-depth below.

Local Field Potential

Trial-averaged spectrograms and coherograms were calculated using multi-taper spectral methods included in the Chronux package for MATLAB (www.chronux.org). To get the beta filtered local field potential (LFP) signal, raw LFP (with respect to GND) was band pass filtered at 20-30 Hz using a zero-phase IIR filter. Amplitude, phase, and envelope magnitude of the signals were obtained using a Hilbert transform. Beta power and coherence were z-scored to the epoch mean. Similarly, the respiratory rhythm signal was obtained by band pass filtering the raw LFP at 7-8 Hz.

Bootstrap Tests

Bootstrap tests for **Supplementary Fig. 3e** were performed when coherence on odor-cued and air-cued trials were compared, to account for the much larger percentage of odor-cued trials. Data points on odor trials were randomly downsampled with replacement to match the number of air trials, and the mean was calculated for this new set of datapoints. This downsampling was done 1000 times, to create a new, bootstrapped distribution of means. The observed mean value for the air trial distribution was compared to the bootstrapped distribution.

724 P-values were calculated by counting the number of values in the bootstrapped distribution that
725 were greater than or equal to the observed mean value, and dividing by the total number of re-
726 samples (1000). P-values less than 0.05 were considered statistically significant, and thus
727 rejected the null hypothesis that the two observed distributions had equal means.

728

729 **Sharp-Wave Ripple Detection**

730 Hippocampal sharp-wave ripples were detected as previously described (Jadhav et al.,
731 2016; Shin et al., 2019; Tang et al., 2017). Briefly, the locally referenced LFP signal from CA1
732 tetrodes was filtered in the ripple band (150-250 Hz), and the envelope of the ripple-filtered
733 LFPs was determined using a Hilbert transform. SWR events were detected as contiguous
734 periods when the envelope stayed above 3 SD of the mean on at least one tetrode for at least
735 15 ms.

736

737 **Cross-frequency Coupling**

738 Phase-amplitude coupling between RR and beta was computed for **Supplementary Fig.**
739 **2f** as previously described (Tort et al., 2010). In brief, the phases of RR were divided into 20
740 degree bins, and the mean amplitude of the beta rhythm at each phase was calculated. The
741 mean amplitudes were then normalized by dividing each bin by the sum of amplitudes across all
742 bins. The strength of phase-amplitude coupling was determined by comparing the amplitude
743 distribution to a uniform distribution by calculating the modulation index (MI), which is based on
744 the Kullback–Leibler (KL) distance but normalized so that values fall between 0 and 1, where a
745 value of 0 indicates a uniform distribution of beta amplitudes across RR phases. Significance

was determined by comparing the calculated MI to a null distribution generated by shuffling the trial number assignments of the RR phase series; this maintains the structure of the underlying rhythm but randomly aligns the beta amplitudes on each trial to each trial sequence RR phases.

Single Unit Analysis

Spike sorting was done semi-automatically using MountainSort (Barnett et al., 2016; Chung et al., 2017), with manual curation. Only well-isolated units were used for analysis. Putative interneurons and pyramidal cells were classified based on average firing rate and spike width, as described previously (Shin et al., 2019; Tang et al., 2017). Units were classified as interneurons if they had an average firing rate exceeding 7 Hz and an average spike width under 0.3 ms. All other units were considered putative pyramidal cells. Units were excluded from analysis if they had fewer than 100 spikes across all sessions. A small number of pyramidal cells only had spikes during sleep epochs, and these were excluded from analysis (Jadhav et al., 2016; Karlsson and Frank, 2009) since all analysis done here focused exclusively on the task periods.

Task Responsiveness

Task responsiveness was calculated as a change in firing rate following odor onset, compared to a pre-stimulus period of the same length of time as the odor sampling period on each trial leading up to odor port engagement. Sampling events were only considered if the animal held its nose in the odor port for longer than 0.50 seconds and proceeded to a reward port. Statistical significance was determined from the Wilcoxon signed rank test of those trial-matched rate differences for each odor identity separately. If a cell showed a significant change

up or down from baseline for at least one of the odors, it was considered task responsive. Of note, there was only a single unit analyzed whose firing rate changed in opposite directions from baseline for the two odors, the remainder showed the same direction of change in firing rate for the two odors.

Choice Selectivity

Firing rates during odor sampling were calculated as the number of spikes as a function of time from odor-port engagement to odor-port disengagement. Choice selectivity was calculated using the following equation:

$$SI = \frac{\lambda_1 - \lambda_2}{\lambda_1 + \lambda_2}$$

Where λ_1 is the firing rate vector for Odor 1 trials, and λ_2 is firing rate vector for Odor 2 trials. *SI* = 1 indicates that the cell only responded on Odor 1 trials, whereas *SI* = -1 indicates that the cell only responded on Odor 2 trials. To determine significance, a null distribution was generated in which the odor identities were shuffled across trials. Cells were considered choice-selective if the SI fell outside of 1.5 s.d. from the mean of the null distribution.

Corrected Spike Cross- Correlogram

To correct for the triangular shape in the cross correlogram, we utilized a spike-shuffling procedure similar to that previously described (Kay et al., 2020). In brief, all spikes from one cell were jittered +/- 50 msec and the cross correlogram was recalculated from -.15 seconds to .15 seconds in 2.5 msec bins. This procedure was performed 1000 times, and the pointwise zscore

790 of the real cross-correlogram was calculated. The highest peak within +/- 100 msec that
791 achieved significance ($p<.05$), was chosen as the significant peak in the ccg, and only those
792 cross correlograms in which there was a significant peak were displayed (and smoothed with a
793 Gaussian kernel with $\sigma=1$ bin).

794

795 **Phase Locking**

796 For all phase-locking analyses, the tetrode in each region with the most cells on each
797 given day was used to measure oscillatory phase of either beta or RR. Phase locking of
798 individual cells to the beta and respiratory rhythms was calculated by pooling the spike phases
799 of each cell during the odor-sampling periods and performing a Rayleigh Z test for circular non-
800 uniformity. When comparing phase coherence during correct trials versus that during incorrect
801 trials, we adopted a down sampling strategy to adjust for rate differences, as described
802 previously (Rangel et al., 2016). First, we matched the number of spikes during correct trials to
803 that during incorrect trials. We then bootstrapped a mean vector length for the downsampled
804 correct trials 1000 times and directly compared that to the MVL during incorrect trials. For
805 calculation of the mean phase preference of each cell, we calculated the mean phase of all
806 spikes during correct trials assuming a von-mises distribution.

807

808 **Principal Component Analysis (PCA)**

809 We used PCA to visualize population activity of CA1 and PFC ensembles over time individual
810 sessions. Spiking activity in the decision making period aligned to odor onset was binned
811 (binsize = 100 ms, window = 0-1 s), and a firing rate matrix was constructed where each row
812 represents a bin and each column represents a neuron. Only sessions with at least 4 task-

813 responsive neurons (threshold applied for both CA1 and PFC; CA1 and PFC ensembles were
814 examined separately) were used for analyses. We used PCA to find the principal component
815 coefficients of the matrix, and applied the coefficients to the population activity for left-bond vs.
816 right-bound trials. Population activity was projected onto the PC space. The first 3 PCs were
817 used for visualization and analysis. The Euclidean distance between left-bound and right-bound
818 average trajectories was compared to a chance-level distance distribution computed by shuffling
819 the trial identities across trials and creating a null distribution. The timepoint at which the
820 population responses were considered significantly distinct from each other was defined as the
821 first timepoint at which the real distance between trajectories surpassed the 95% confidence
822 interval of the null (shuffled) distribution. Similar results were obtained for Euclidean distance
823 computed with the first 3 PCs and for Euclidean distance computed for all neurons without
824 dimensionality reduction.

825

826 **GLM**

827 A generalized linear model (GLM) with a log link function was constructed to predict
828 reward choice based on neural activity during the odor sampling period. Activity from all task-
829 responsive neurons that were active on at least 10 trials was included. Neural population activity
830 from different length time bins from 0.1 seconds to 1 second aligned to odor onset was used for
831 prediction, i.e. 0-0.1s, 0-0.2s … 0-1.0s. Five-fold cross validation was used to test prediction.
832 For each fold, the session's trials were randomly partitioned into five equally sized sets. Four of
833 the five sets were used to train the GLM model and the remaining set was used to test. The
834 prediction accuracy was calculated by dividing the number of correctly predicted trials by the
835 total number of trials used for testing for each fold.

836 Significance was determined by performing the same procedure as described above but
837 shuffling the trial outcomes to obtain a null distribution. At each time bin used for the prediction,
838 a rank-sum test was performed on the prediction accuracy using the real data compared to the
839 shuffled data.

840

841 **Occupancy Maps**

842 For all spatial field analyses, only the 5 animals that were trained on the full T-maze
843 were used; the three animals trained on the truncated maze were excluded due to insufficient
844 spatial data. Two-dimensional occupancy maps were generated by calculating occupancy in 2-
845 cm square spatial bins from epochs in which the animals running speed exceeded 3 cm/sec and
846 convolving with a 2d Gaussian ($\boldsymbol{\sigma}$= 2 pixels).

847

848 **Place Field Determination**

849 2-D occupancy-normalized firing rate maps were generated by dividing the spikes at
850 each 2-D pixel by the unsmoothed occupancy at that pixel, and then smoothing with a Gaussian
851 kernel of (σ= 2 pixels, or 4 cm).

852 Linearized trajectory occupancy maps were calculated as previously described[31,97,98]. Briefly,
853 the rats 2d spatial coordinates were first segmented into run epochs based on contiguous bouts
854 of time in which the animals running speed exceeded 3 cm/sec. Then, the position of the animal
855 during each 'run epoch' was categorized by its origin and destination, and each position was
856 assigned to one of 100 (1.23 cm) bins from the origin to the destination of that route. Then the
857 total number of spikes at each bin was divided by that bin's occupancy, and the map was
858 convolved by a Gaussian kernel with a standard deviation of 2 pixels (4 cm).

859 Place field peak was calculated as the peak rate bin on the smoothed, linearized rate map,
860 and place fields were only considered for trajectories in which the cell had a peak firing rate of at
861 least 1 Hz. Place field width was calculated using a flood fill-algorithm in which the edges were
862 defined as the closest bins to the peak bin in which the rate fell below 25% of the peak rate.
863 Place field sparsity and information scores were calculated as previously described (Skaggs et
864 al., 1993). A cell was determined to have a place field if its peak firing rate along that trajectory
865 was ≥ 2 S.D. above the mean of a bootstrapped distribution generated by circularly shifting the
866 spikes in time for each individual run, and if the field covered less than 75% of the linearized
867 trajectory. When analyzing the place field characteristics of choice-selective cells (**Fig. 7**,
868 **Supplementary Fig. 6**), the field of each outbound journey was analyzed separately so as to
869 prevent 'choosing' certain fields over others.

870

871 **Trajectory Selectivity**

872 Trajectory selective cells were identified using a previously validated method (Shin et al.,
873 2019). Briefly, the linearized spatial tuning curve was calculated separately for each outbound
874 trajectory and the correlation between those trajectories was computed. A cell was identified as
875 trajectory selective if this correlation value exceeded the 95th percentile of a distribution wherein
876 each outbound trajectory identity was shuffled and the correlation recalculated.

877 To measure trajectory selectivity as it related to decision period selectivity, we used an
878 analogous method to the odor selectivity index. Briefly, we calculated the mean firing rate along
879 each run beginning one half second following odor port exit and once the animal's speed
880 exceeded 3 cm/sec to the end of that run (when the animal either reached the goal or its
881 velocity fell below 3 cm/sec for more than ½ second). The difference in these mean firing rates

across runs was divided by the sum of those two mean rates to generate a trajectory selectivity index.

Bayesian Decoder

Choice identity decoding was performed as previously described (Karlsson and Frank, 2009). Briefly, a memoryless Bayesian decoder was built for each of the two choice identities from spikes occurring in the odor sampling period. Then, the likelihood of each choice (x) was reconstructed from their posterior probabilities given the spikes occurring at each segment along the maze on each run (p(x | spikes) = p(spikes | x) * p(x) / p(spikes)). Run activity was defined as contiguous bouts following the odor sampling period when the animal was traveling above 3 cm/sec. Additionally, to prevent overlap between odor-period spiking and run spiking, the run periods were defined beginning 0.5 seconds following odor port disengagement time. We assumed that the N active cells fired independently and followed a Poisson process, giving the following equation.

$$P(X|spikes) = C * (\prod_{i=1}^{N} f_i(X)^{spikes_i}) * e^{-\tau} \sum_{i=1}^{N} f(X)$$

Where C is a normalization constant across the two choice identities. The p-value was calculated from the Gaussian statistics of a Monte Carlo random shuffle (200 shuffles) of choice identity during the odor sampling period. When choice identity decoding was calculated from the likelihoods of activity from each run, the decoding was performed in the same 5-fold leave-one-out fashion as was used in the GLM analyses, and the p value was calculated from the same Monte Carlo random shuffle of the training set route identities as the odor period based decoding.

Data Availability

The behavioral and electrophysiological data supporting the findings in this study are archived on servers at Brandeis University and are available upon request to the corresponding author.

Code Availability

All data processing, analyses and statistics in this study were conducted using open-source package Mountainsort (https://github.com/flatironinstitute/mountainsort) and custom code in MATLAB (R2018), unless otherwise noted. All custom code is available on GitHub and upon request to the corresponding author.

ACKNOWLEDGMENTS

This work was supported by NIH Grant R01MH120228, and a Smith Foundation Odyssey award to S.P.J. We thank the late Howard Eichenbaum for assistance with the behavioral task.

AUTHOR CONTRIBUTIONS

SPJ: Conception and Study Design, Data Analysis; CAS: Experiments, Data Analysis, JHB: Data Analysis, EK: Experiments, PM: Data Analysis. SPJ, CAS and JHB wrote the manuscript with input from all authors.

COMPETING INTERESTS STATEMENT

The authors declare no competing interests.

REFERENCES

Abraham, N.M., Spors, H., Carleton, A., Margrie, T.W., Kuner, T., and Schaefer, A.T. (2004). Maintaining accuracy at the expense of speed: stimulus similarity defines odor discrimination time in mice. Neuron *44*, 865-876.

Allen, T.A., Salz, D.M., McKenzie, S., and Fortin, N.J. (2016). Nonspatial Sequence Coding in CA1 Neurons. J Neurosci *36*, 1547-1563.

Alvarez, P., Wendelken, L., and Eichenbaum, H. (2002). Hippocampal formation lesions impair performance in an odor-odor association task independently of spatial context. NeurobiolLearnMem *78*, 470-476.

Andrianova, L., Brady, E.S., Margetts-Smith, G., Kohli, S., McBain, C.J., and Craig, M.T. (2021). Hippocampal CA1 pyramidal cells do not receive monosynaptic input from thalamic nucleus reuniens. bioRxiv, 2021.2009.2030.462517.

Barnett, A.H., Magland, J.F., and Greengard, L.F. (2016). Validation of neural spike sorting algorithms without ground-truth information. J Neurosci Methods *264*, 65-77.

Battaglia, F.P., Benchenane, K., Sirota, A., Pennartz, C.M., and Wiener, S.I. (2011). The hippocampus: hub of brain network communication for memory. Trends Cogn Sci *15*, 310-318.

Benchenane, K., Peyrache, A., Khamassi, M., Tierney, P.L., Gioanni, Y., Battaglia, F.P., and Wiener, S.I. (2010). Coherent theta oscillations and reorganization of spike timing in the hippocampal-prefrontal network upon learning. Neuron *66*, 921-936.

Benchenane, K., Tiesinga, P.H., and Battaglia, F.P. (2011). Oscillations in the prefrontal cortex: a gateway to memory and attention. Curr Opin Neurobiol *21*, 475-485.

Beshel, J., Kopell, N., and Kay, L.M. (2007). Olfactory bulb gamma oscillations are enhanced with task demands. J Neurosci *27*, 8358-8365.

Buschman, T.J., Denovellis, E.L., Diogo, C., Bullock, D., and Miller, E.K. (2012). Synchronous oscillatory neural ensembles for rules in the prefrontal cortex. Neuron *76*, 838-846.

Buzsáki, G. (2015). Hippocampal sharp wave-ripple: A cognitive biomarker for episodic memory and planning. Hippocampus *25*, 1073-1188.

Buzsaki, G., and Draguhn, A. (2004). Neuronal oscillations in cortical networks. Science *304*, 1926-1929.

Buzsaki, G., Leung, L.W., and Vanderwolf, C.H. (1983). Cellular bases of hippocampal EEG in the behaving rat. Brain Res *287*, 139-171.

Carr, M.F., Jadhav, S.P., and Frank, L.M. (2011). Hippocampal replay in the awake state: a potential substrate for memory consolidation and retrieval. Nat Neurosci *14*, 147-153.

Cenquizca, L.A., and Swanson, L.W. (2007). Spatial organization of direct hippocampal field CA1 axonal projections to the rest of the cerebral cortex. Brain Res Rev *56*, 1-26.

Chung, J.E., Magland, J.F., Barnett, A.H., Tolosa, V.M., Tooker, A.C., Lee, K.Y., Shah, K.G., Felix, S.H., Frank, L.M., and Greengard, L.F. (2017). A Fully Automated Approach to Spike Sorting. Neuron *95*, 1381-1394 e1386.

Churchwell, J.C., Morris, A.M., Musso, N.D., and Kesner, R.P. (2010). Prefrontal and hippocampal contributions to encoding and retrieval of spatial memory. Neurobiol Learn Mem *93*, 415-421.

Colgin, L.L. (2011). Oscillations and hippocampal-prefrontal synchrony. Curr Opin Neurobiol *21*, 467-474.

Delatour, B., and Witter, M.P. (2002). Projections from the parahippocampal region to the prefrontal cortex in the rat: evidence of multiple pathways. Eur J Neurosci *15*, 1400--1407.

DeNardo, L.A., Liu, C.D., Allen, W.E., Adams, E.L., Friedmann, D., Fu, L., Guenthner, C.J., Tessier-Lavigne, M., and Luo, L. (2019). Temporal evolution of cortical ensembles promoting remote memory retrieval. Nat Neurosci *22*, 460-469.

Dolleman-van der Weel, M.J., Griffin, A.L., Ito, H.T., Shapiro, M.L., Witter, M.P., Vertes, R.P., and Allen, T.A. (2019). The nucleus reuniens of the thalamus sits at the nexus of a hippocampus and medial prefrontal cortex circuit enabling memory and behavior. Learn Mem *26*, 191-205.

Donoghue, J.P., Sanes, J.N., Hatsopoulos, N.G., and Gaal, G. (1998). Neural discharge and local field potential oscillations in primate motor cortex during voluntary movements. J Neurophysiol *79*, 159-173.

Eichenbaum, H. (1998). Using olfaction to study memory. Ann N Y Acad Sci *855*, 657-669.

Eichenbaum, H., Fagan, A., and Cohen, N.J. (1986). Normal olfactory discrimination learning set and facilitation of reversal learning after medial-temporal damage in rats: implications for an account of preserved learning abilities in amnesia. J Neurosci *6*, 1876-1884.

Eichenbaum, H., Kuperstein, M., Fagan, A., and Nagode, J. (1987). Cue-sampling and goal-approach correlates of hippocampal unit activity in rats performing an odor-discrimination task. J Neurosci *7*, 716-732.

Euston, D.R., Gruber, A.J., and McNaughton, B.L. (2012). The role of medial prefrontal cortex in memory and decision making. Neuron *76*, 1057-1070.

Ferbinteanu, J., Shirvalkar, P., and Shapiro, M.L. (2011). Memory modulates journey-dependent coding in the rat hippocampus. J Neurosci *31*, 9135-9146.

Fitzgerald, J.K., Freedman, D.J., and Assad, J.A. (2011). Generalized associative representations in parietal cortex. Nat Neurosci *14*, 1075-1079.

Floresco, S.B., Seamans, J.K., and Phillips, A.G. (1997). Selective roles for hippocampal, prefrontal cortical, and ventral striatal circuits in radial-arm maze tasks with or without a delay. J Neurosci *17*, 1880-1890.

Fortin, N.J., Wright, S.P., and Eichenbaum, H. (2004). Recollection-like memory retrieval in rats is dependent on the hippocampus. Nature *431*, 188-191.

Frederick, D.E., Brown, A., Brim, E., Mehta, N., Vujovic, M., and Kay, L.M. (2016). Gamma and Beta Oscillations Define a Sequence of Neurocognitive Modes Present in Odor Processing. J Neurosci *36*, 7750-7767.

Fujisawa, S., Amarasingham, A., Harrison, M.T., and Buzsaki, G. (2008). Behavior-dependent short-term assembly dynamics in the medial prefrontal cortex. Nat Neurosci *11*, 823-833.

Fujisawa, S., and Buzsaki, G. (2011). A 4 Hz oscillation adaptively synchronizes prefrontal, VTA, and hippocampal activities. Neuron *72*, 153-165.

Gordon, J.A. (2011). Oscillations and hippocampal-prefrontal synchrony. Curr Opin Neurobiol *21*, 486-491.

Gothard, K.M., Skaggs, W.E., Moore, K.M., and McNaughton, B.L. (1996). Binding of hippocampal CA1 neural activity to multiple reference frames in a landmark-based navigation task. Journal of Neuroscience *16*, 823-835.

Harvey, C.D., Coen, P., and Tank, D.W. (2012). Choice-specific sequences in parietal cortex during a virtual-navigation decision task. Nature *484*, 62-68.

Hasegawa, I. (2000). Neural mechanisms of memory retrieval: role of the prefrontal cortex. Rev Neurosci *11*, 113-125.

Hermer-Vazquez, R., Hermer-Vazquez, L., Srinivasan, S., and Chapin, J.K. (2007). Beta- and gamma-frequency coupling between olfactory and motor brain regions prior to skilled, olfactory-driven reaching. Exp Brain Res *180*, 217-235.

Hyman, J.M., Ma, L., Balaguer-Ballester, E., Durstewitz, D., and Seamans, J.K. (2012). Contextual encoding by ensembles of medial prefrontal cortex neurons. Proc Natl Acad Sci U S A *109*, 5086-5091.

Hyman, J.M., Zilli, E.A., Paley, A.M., and Hasselmo, M.E. (2010). Working Memory Performance Correlates with Prefrontal-Hippocampal Theta Interactions but not with Prefrontal Neuron Firing Rates. Frontiers in integrative neuroscience *4*, 2.

Igarashi, K.M., Lu, L., Colgin, L.L., Moser, M.B., and Moser, E.I. (2014). Coordination of entorhinal-hippocampal ensemble activity during associative learning. Nature *510*, 143-147.

Ito, H.T., Zhang, S.J., Witter, M.P., Moser, E.I., and Moser, M.B. (2015). A prefrontal-thalamo-hippocampal circuit for goal-directed spatial navigation. Nature *522*, 50-55.

1029 Jadhav, S.P., Kemere, C., German, P.W., and Frank, L.M. (2012). Awake hippocampal sharp-
1030 wave ripples support spatial memory. Science *336*, 1454-1458.

1031 Jadhav, S.P., Rothschild, G., Roumis, D.K., and Frank, L.M. (2016). Coordinated excitation and
1032 inhibition of prefrontal ensembles during awake hippocampal sharp-wave ripple events. Neuron
1033 *90*, 113-127.

1034 Johnson, A., and Redish, A.D. (2007). Neural ensembles in CA3 transiently encode paths
1035 forward of the animal at a decision point. Journal of Neuroscience *27*, 12176-12189.

1036 Jones, M.W., and Wilson, M.A. (2005). Theta rhythms coordinate hippocampal-prefrontal
1037 interactions in a spatial memory task. PLoSBiol *3*, e402.

1038 Joo, H.R., and Frank, L.M. (2018). The hippocampal sharp wave-ripple in memory retrieval for
1039 immediate use and consolidation. Nat Rev Neurosci *19*, 744-757.

1040 Karalis, N., and Sirota, A. (2022). Breathing coordinates cortico-hippocampal dynamics in mice
1041 during offline states. Nat Commun *13*, 467.

1042 Karlsson, M.P., and Frank, L.M. (2009). Awake replay of remote experiences in the
1043 hippocampus. Nat Neurosci *12*, 913-918.

1044 Kay, K., Chung, J.E., Sosa, M., Schor, J.S., Karlsson, M.P., Larkin, M.C., Liu, D.F., and Frank,
1045 L.M. (2020). Constant Sub-second Cycling between Representations of Possible Futures in the
1046 Hippocampus. Cell *180*, 552-567 e525.

1047 Kay, L.M. (2005). Theta oscillations and sensorimotor performance. ProcNatlAcadSciUSA *102*,
1048 3863-3868.

1049 Kay, L.M. (2014). Circuit oscillations in odor perception and memory. Prog Brain Res *208*, 223-
1050 251.

1051 Kay, L.M., and Beshel, J. (2010). A beta oscillation network in the rat olfactory system during a
1052 2-alternative choice odor discrimination task. J Neurophysiol *104*, 829-839.

1053 Kay, L.M., Beshel, J., Brea, J., Martin, C., Rojas-Libano, D., and Kopell, N. (2009). Olfactory
1054 oscillations: the what, how and what for. Trends Neurosci *32*, 207-214.

1055 Kepecs, A., Uchida, N., and Mainen, Z.F. (2006). The sniff as a unit of olfactory processing.
1056 Chem Senses *31*, 167-179.

1057 Komorowski, R.W., Manns, J.R., and Eichenbaum, H. (2009). Robust conjunctive item-place
1058 coding by hippocampal neurons parallels learning what happens where. J Neurosci *29*, 9918-
1059 9929.

1060 Lee, I., and Solivan, F. (2008). The roles of the medial prefrontal cortex and hippocampus in a
1061 spatial paired-association task. Learn Mem *15*, 357-367.

1062 Lisman, J.E., and Jensen, O. (2013). The θ-γ neural code. Neuron *77*, 1002-1016.

1063 Liu, X., Ramirez, S., Pang, P.T., Puryear, C.B., Govindarajan, A., Deisseroth, K., and
1064 Tonegawa, S. (2012). Optogenetic stimulation of a hippocampal engram activates fear memory
1065 recall. Nature *484*, 381-385.

1066 Lockmann, A.L., Laplagne, D.A., Leao, R.N., and Tort, A.B. (2016). A Respiration-Coupled
1067 Rhythm in the Rat Hippocampus Independent of Theta and Slow Oscillations. J Neurosci *36*,
1068 5338-5352.

1069 Maharjan, D.M., Dai, Y.Y., Glantz, E.H., and Jadhav, S.P. (2018). Disruption of dorsal
1070 hippocampal - prefrontal interactions using chemogenetic inactivation impairs spatial learning.
1071 Neurobiol Learn Mem *155*, 351-360.

1072 Martin, C., Beshel, J., and Kay, L.M. (2007). An olfacto-hippocampal network is dynamically
1073 involved in odor-discrimination learning. J Neurophysiol *98*, 2196-2205.

1074 Martin, C., Gervais, R., Messaoudi, B., and Ravel, N. (2006). Learning-induced oscillatory
1075 activities correlated to odour recognition: a network activity. Eur J Neurosci *23*, 1801-1810.

1076 McKenzie, S., Frank, A.J., Kinsky, N.R., Porter, B., Riviere, P.D., and Eichenbaum, H. (2014).
1077 Hippocampal representation of related and opposing memories develop within distinct,
1078 hierarchically organized neural schemas. Neuron *83*, 202-215.

1079 Miller, E.K., and Cohen, J.D. (2001). An integrative theory of prefrontal cortex function. Annu
1080 Rev Neurosci *24*, 167-202.

1081 Moita, M.A., Rosis, S., Zhou, Y., LeDoux, J.E., and Blair, H.T. (2003). Hippocampal place cells
1082 acquire location-specific responses to the conditioned stimulus during auditory fear conditioning.
1083 Neuron *37*, 485-497.

1084 Moser, M.B., and Moser, E.I. (1998). Distributed encoding and retrieval of spatial memory in the
1085 hippocampus. J Neurosci *18*, 7535--7542.

1086 Neville, K.R., and Haberly, L.B. (2003). Beta and gamma oscillations in the olfactory system of
1087 the urethane-anesthetized rat. J Neurophysiol *90*, 3921-3930.

1088 Nguyen Chi, V., Muller, C., Wolfenstetter, T., Yanovsky, Y., Draguhn, A., Tort, A.B., and
1089 Brankack, J. (2016). Hippocampal Respiration-Driven Rhythm Distinct from Theta Oscillations in
1090 Awake Mice. J Neurosci *36*, 162-177.

1091 Norman, Y., Yeagle, E.M., Khuvis, S., Harel, M., Mehta, A.D., and Malach, R. (2019).
1092 Hippocampal sharp-wave ripples linked to visual episodic recollection in humans. Science *365*.

1093 Otto, T., and Eichenbaum, H. (1992a). Complementary roles of the orbital prefrontal cortex and
1094 the perirhinal- entorhinal cortices in an odor-guided delayed-nonmatching-to-sample task.
1095 BehavNeurosci *106*, 762-775.

1096 Otto, T., and Eichenbaum, H. (1992b). Neuronal activity in the hippocampus during delayed
1097 non-match to sample performance in rats: evidence for hippocampal processing in recognition
1098 memory. Hippocampus *2*, 323-334.

Papale, A.E., Zielinski, M.C., Frank, L.M., Jadhav, S.P., and Redish, A. (2016). Interplay between Hippocampal Sharp-Wave-Ripple Events and Vicarious Trial and Error Behaviors in Decision Making. Neuron *92*, 975-982.

Peters, G.J., David, C.N., Marcus, M.D., and Smith, D.M. (2013). The medial prefrontal cortex is critical for memory retrieval and resolving interference. Learn Mem *20*, 201-209.

Place, R., Farovik, A., Brockmann, M., and Eichenbaum, H. (2016). Bidirectional prefrontal-hippocampal interactions support context-guided memory. Nat Neurosci.

Rangel, L.M., Rueckemann, J.W., Riviere, P.D., Keefe, K.R., Porter, B.S., Heimbuch, I.S., Budlong, C.H., and Eichenbaum, H. (2016). Rhythmic coordination of hippocampal neurons during associative memory processing. eLife *5*.

Rinberg, D., Koulakov, A., and Gelperin, A. (2006). Speed-accuracy tradeoff in olfaction. Neuron *51*, 351-358.

Schlecht, M., Jayachandran, M., Rasch, G.E., and Allen, T.A. (2022). Dual projecting cells linking thalamic and cortical communication routes between the medial prefrontal cortex and hippocampus. Neurobiol Learn Mem *188*, 107586.

Schoenbaum, G., and Eichenbaum, H. (1995a). Information coding in the rodent prefrontal cortex. I. Single-neuron activity in orbitofrontal cortex compared with that in pyriform cortex. JNeurophysiol *74*, 733-750.

Schoenbaum, G., and Eichenbaum, H. (1995b). Information coding in the rodent prefrontal cortex. II. Ensemble activity in orbitofrontal cortex. JNeurophysiol *74*, 751-762.

Shadlen, M.N., and Newsome, W.T. (2001). Neural basis of a perceptual decision in the parietal cortex (area LIP) of the rhesus monkey. J Neurophysiol *86*, 1916-1936.

Shin, J.D., and Jadhav, S.P. (2016). Multiple modes of hippocampal-prefrontal interactions in memory-guided behavior. Curr Opin Neurobiol *40*, 161-169.

Shin, J.D., Tang, W., and Jadhav, S.P. (2019). Dynamics of Awake Hippocampal-Prefrontal Replay for Spatial Learning and Memory-Guided Decision Making. Neuron *104*, 1110–1125.e1117.

Siapas, A.G., Lubenov, E.V., and Wilson, M.A. (2005). Prefrontal phase locking to hippocampal theta oscillations. Neuron *46*, 141-151.

Siegle, J.H., and Wilson, M.A. (2014). Enhancement of encoding and retrieval functions through theta phase-specific manipulation of hippocampus. eLife *3*, e03061.

Singer, A.C., Carr, M.F., Karlsson, M.P., and Frank, L.M. (2013). Hippocampal SWR activity predicts correct decisions during the initial learning of an alternation task. Neuron *77*, 1163-1173.

Skaggs, W.E., McNaughton, B.L., Gothard, K., and Markus, E. (1993). An information theoretic approach to deciphering the hippocampal code. In Advanced in Neural Information Processing Systems, S. Hanson, J.D. Cowan, and C.L. Giles, eds. (San Mateo, CA: Morgan Kaufmann Publishers), pp. 1030-1037.

Stopfer, M., Jayaraman, V., and Laurent, G. (2003). Intensity versus identity coding in an olfactory system. Neuron *39*, 991-1004.

Tang, W., Shin, J.D., Frank, L.M., and Jadhav, S.P. (2017). Hippocampal-prefrontal reactivation during learning is stronger in awake compared with sleep states. J Neurosci *37*, 11789-11805.

Tang, W., Shin, J.D., and Jadhav, S.P. (2021). Multiple time-scales of decision-making in the hippocampus and prefrontal cortex. eLife *10*.

Taxidis, J., Pnevmatikakis, E.A., Dorian, C.C., Mylavarapu, A.L., Arora, J.S., Samadian, K.D., Hoffberg, E.A., and Golshani, P. (2020). Differential Emergence and Stability of Sensory and Temporal Representations in Context-Specific Hippocampal Sequences. Neuron *108*, 984-998 e989.

Terada, S., Sakurai, Y., Nakahara, H., and Fujisawa, S. (2017). Temporal and Rate Coding for Discrete Event Sequences in the Hippocampus. Neuron *94*, 1248-1262 e1244.

Tort, A.B., Komorowski, R., Eichenbaum, H., and Kopell, N. (2010). Measuring phase-amplitude coupling between neuronal oscillations of different frequencies. J Neurophysiol *104*, 1195-1210.

Tort, A.B., Komorowski, R.W., Manns, J.R., Kopell, N.J., and Eichenbaum, H. (2009). Theta-gamma coupling increases during the learning of item-context associations. Proc Natl Acad Sci U S A *106*, 20942-20947.

Uchida, N., and Mainen, Z.F. (2003). Speed and accuracy of olfactory discrimination in the rat. Nat Neurosci *6*, 1224-1229.

Varela, C., Kumar, S., Yang, J.Y., and Wilson, M.A. (2014). Anatomical substrates for direct interactions between hippocampus, medial prefrontal cortex, and the thalamic nucleus reuniens. Brain Struct Funct *219*, 911-929.

Verhagen, J.V., Wesson, D.W., Netoff, T.I., White, J.A., and Wachowiak, M. (2007). Sniffing controls an adaptive filter of sensory input to the olfactory bulb. Nat Neurosci *10*, 631-639.

Wiener, S.I., Paul, C.A., and Eichenbaum, H. (1989). Spatial and behavioral correlates of hippocampal neuronal activity. Journal of Neuroscience *9*, 2737-2763.

Wikenheiser, A.M., and Redish, A. (2015). Hippocampal theta sequences reflect current goals. Nat Neurosci *18*, 289-294.

Wiltgen, B.J., Brown, R.A., Talton, L.E., and Silva, A.J. (2004). New circuits for old memories: the role of the neocortex in consolidation. Neuron *44*, 101-108.

Wiltgen, B.J., Zhou, M., Cai, Y., Balaji, J., Karlsson, M.G., Parivash, S.N., Li, W., and Silva, A.J. (2010). The hippocampus plays a selective role in the retrieval of detailed contextual memories. Curr Biol *20*, 1336-1344.

Wirth, S., Avsar, E., Chiu, C.C., Sharma, V., Smith, A.C., Brown, E., and Suzuki, W.A. (2009). Trial outcome and associative learning signals in the monkey hippocampus. Neuron *61*, 930-940.

Wirth, S., Yanike, M., Frank, L.M., Smith, A.C., Brown, E.N., and Suzuki, W.A. (2003). Single neurons in the monkey hippocampus and learning of new associations. Science *300*, 1578-1581.

Yanike, M., Wirth, S., and Suzuki, W.A. (2004). Representation of well-learned information in the monkey hippocampus. Neuron *42*, 477-487.

Yu, J.Y., and Frank, L.M. (2015). Hippocampal-cortical interaction in decision making. Neurobiol Learn Mem *117*, 34-41.

Zhong, W., Ciatipis, M., Wolfenstetter, T., Jessberger, J., Muller, C., Ponsel, S., Yanovsky, Y., Brankack, J., Tort, A.B.L., and Draguhn, A. (2017). Selective entrainment of gamma subbands by different slow network oscillations. Proc Natl Acad Sci U S A *114*, 4519-4524.

Zielinski, M.C., Shin, J.D., and Jadhav, S.P. (2019). Coherent Coding of Spatial Position Mediated by Theta Oscillations in the Hippocampus and Prefrontal Cortex. J Neurosci *39*, 4550-4565.

Zielinski, M.C., Tang, W., and Jadhav, S.P. (2020). The role of replay and theta sequences in mediating hippocampal-prefrontal interactions for memory and cognition. Hippocampus *30*, 60-72.

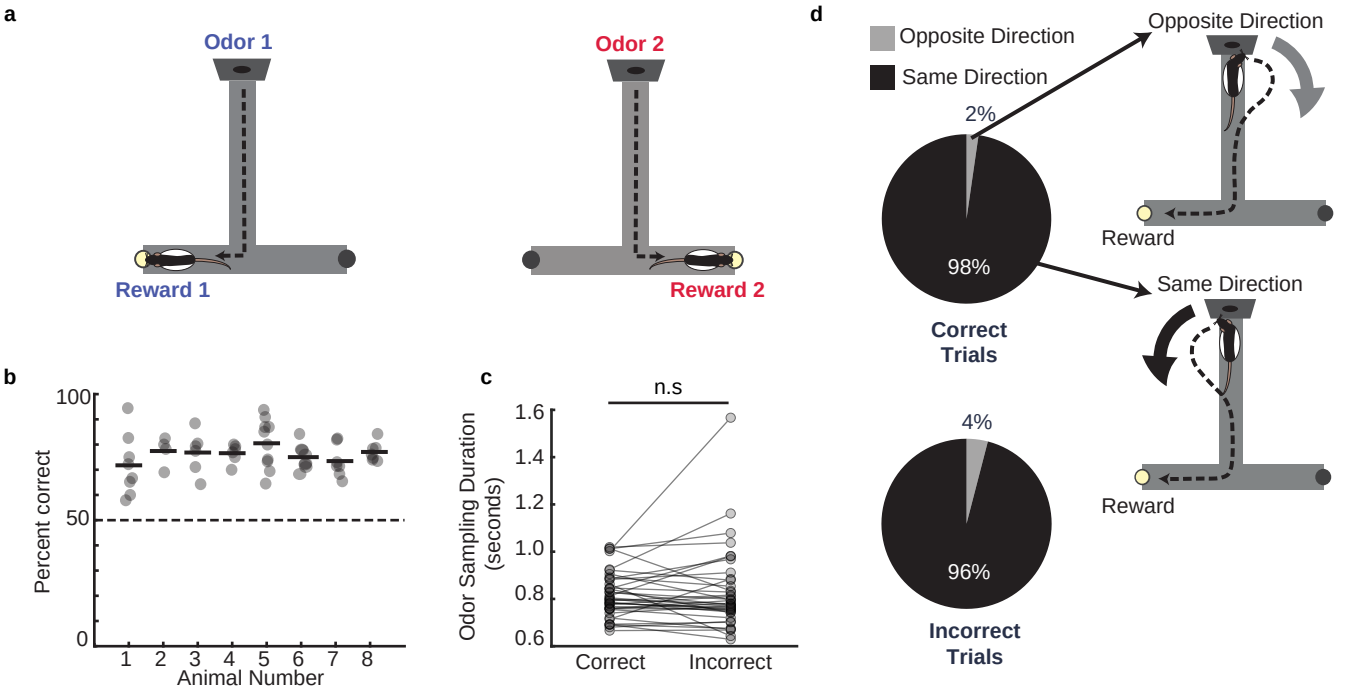
a
Odor 1
Reward 1
Odor 2
Reward 2
b
Percent correct
100
50
0
1 2 3 4 5 6 7 8
Animal Number
c
n.s
Odor Sampling Duration (seconds)
1.6
1.4
1.2
1.0
0.8
0.6
Correct
Incorrect
d
Opposite Direction
Same Direction
2%
98%
Correct Trials
4%
96%
Incorrect Trials
Opposite Direction
Reward
Same Direction
Reward

Figure 1: Odor–place associative memory and decision-making task

a. Schematic of the odor-cued T-maze task. Odors 1 (heptanol) and 2 (ethyl butyrate) were delivered at the odor port in pseudo-random order. Presentation of Odors 1 and 2 was associated with milk reward at Reward locations 1 and 2, respectively. Animals had to recall odor-space associations on each trial and utilize the association to choose the correct reward location.
b. Performance of each animal (*n* = 8) on the odor-cued T-maze task (animals 1 - 5) or truncated odor-cued task (animals 6 - 8; truncated task, without spatial delay period) across multiple sessions (grey dots). Animal average is indicated by black bars. Dashed line indicates chance level.
c. Odor sampling duration across all sessions (n = 38) on correct and incorrect trials (signed-rank test, p = 0.71).
d. Turn direction away from odor port in relation to chosen reward well. Pie charts indicate the fraction of trials in which, at the odor port, animals turned in the same direction versus the opposite direction as the reward well that they would ultimately choose. Sessions in which animals ran the truncated task without spatial delay period were excluded. (correct trials: n = 1624 same direction, 32 opposite direction, binomial test, p = 0; incorrect trials: n = 499 same direction, 21 opposite direction, p = 1.4e-108).

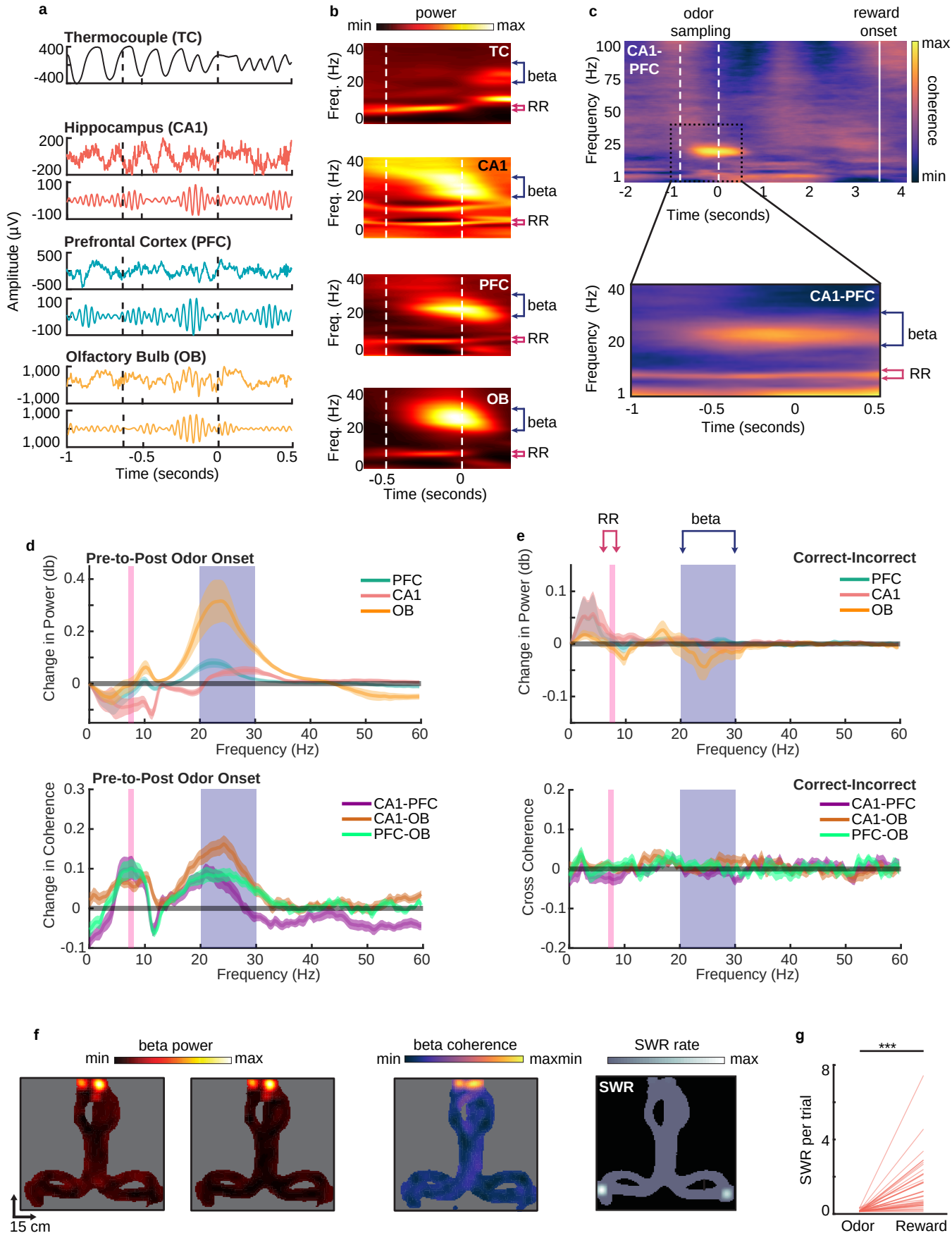
a
Thermocouple (TC)
Hippocampus (CA1)
Prefrontal Cortex (PFC)
Olfactory Bulb (OB)
Amplitude (μV)
Time (seconds)
b
power
min
max
TC
CA1
PFC
OB
beta
RR
Freq. (Hz)
Time (seconds)
c
odor sampling
reward onset
CA1-PFC
Frequency (Hz)
coherence
max
min
Time (seconds)
CA1-PFC
beta
RR
d
Pre-to-Post Odor Onset
Change in Power (db)
PFC
CA1
OB
Frequency (Hz)
Pre-to-Post Odor Onset
Change in Coherence
CA1-PFC
CA1-OB
PFC-OB
e
RR
beta
Correct-Incorrect
Change in Power (db)
Cross Coherence
f
beta power
min
max
beta coherence
maxmin
SWR rate
SWR
15 cm
g
***
SWR per trial
Odor
Reward

Figure 2: Beta rhythms support decision making based on odor-place associations

a. Examples of thermocouple and LFP traces from one tetrode in each region during presentation of odor from one trial, aligned to odor port disengagement. Area between dashed lines indicates odor sampling period. Top to bottom: Respiratory rhythm recorded via thermocouple, CA1 signal, beta band (20-30 Hz) filtered CA1 signal, PFC signal, beta band filtered PFC signal, OB signal, beta band filtered OB signal.
b. Time-frequency plot showing power spectra aligned to odor offset. Color scale represents z-scored power. Area between dashed lines indicates average odor sampling period. Beta band is marked by blue bracket (20-30 Hz). RR band is marked by pink bracket (7-8 Hz). Thermocouple signal (TC), n = 12 sessions, max 0.69, min -0.31; CA1: n = 26 sessions, max 0.26, min -0.35; PFC: n = 26 sessions, max 0.60, min -0.16; and OB: n = 26 sessions, max 2.17, min -0.24.
c. Top: CA1-PFC coherence spectra for one animal during the full task time window from odor sampling (area between white dashed lines, aligned to odor offset) to average reward onset time (solid line) (n = 4 sessions, max 0.84; min -0.41). Bottom: CA1-PFC coherence aligned to odor offset across all animals (n = 38 sessions, max 0.51; min -0.34). Color scale represents z-scored power.
d. Change in PFC, CA1 and OB LFP power(top) and coherence(bottom) from pre odor period to odor period. Beta band shows significant increase in power (signed-rank tests, n = 26 sessions, CA1 p=2.84e-3, PFC p=1.80e-4, OB p=8.3e-6), while both beta and RR bands show significant increase in coherence (signed-rank test, n=26 sessions, beta: CA1-PFC p=2.84e-3, CA1-OB p=5.1e-5, PFC-OB p=3.67e-5; RR: CA1-PFC p=3.94e-3, CA1-OB p=6.35e-4, PFC-OB p=2.43e-4)
e. Change in PFC, CA1 and OB LFP power(top) and coherence(bottom) from incorrect trials to correct trials. No significant changes were detected (signed rank test, n = 26 sessions).
f. Maps of T-maze showing the spatial distribution of z-scored CA1 beta power (left. max 1.49; min -0.19), PFC beta power (middle-left, max 1.63; min -0.18), CA1-PFC beta coherence (middle-right, max 1.16; min -0.19), and SWR rate (right, max 1.34; min 0). Plots are for a single session from one animal.
g. Number of SWR events per trial during odor sampling and reward consumption on correct trials (signed-rank test, n = 38 sessions, p =1.1e-7***).

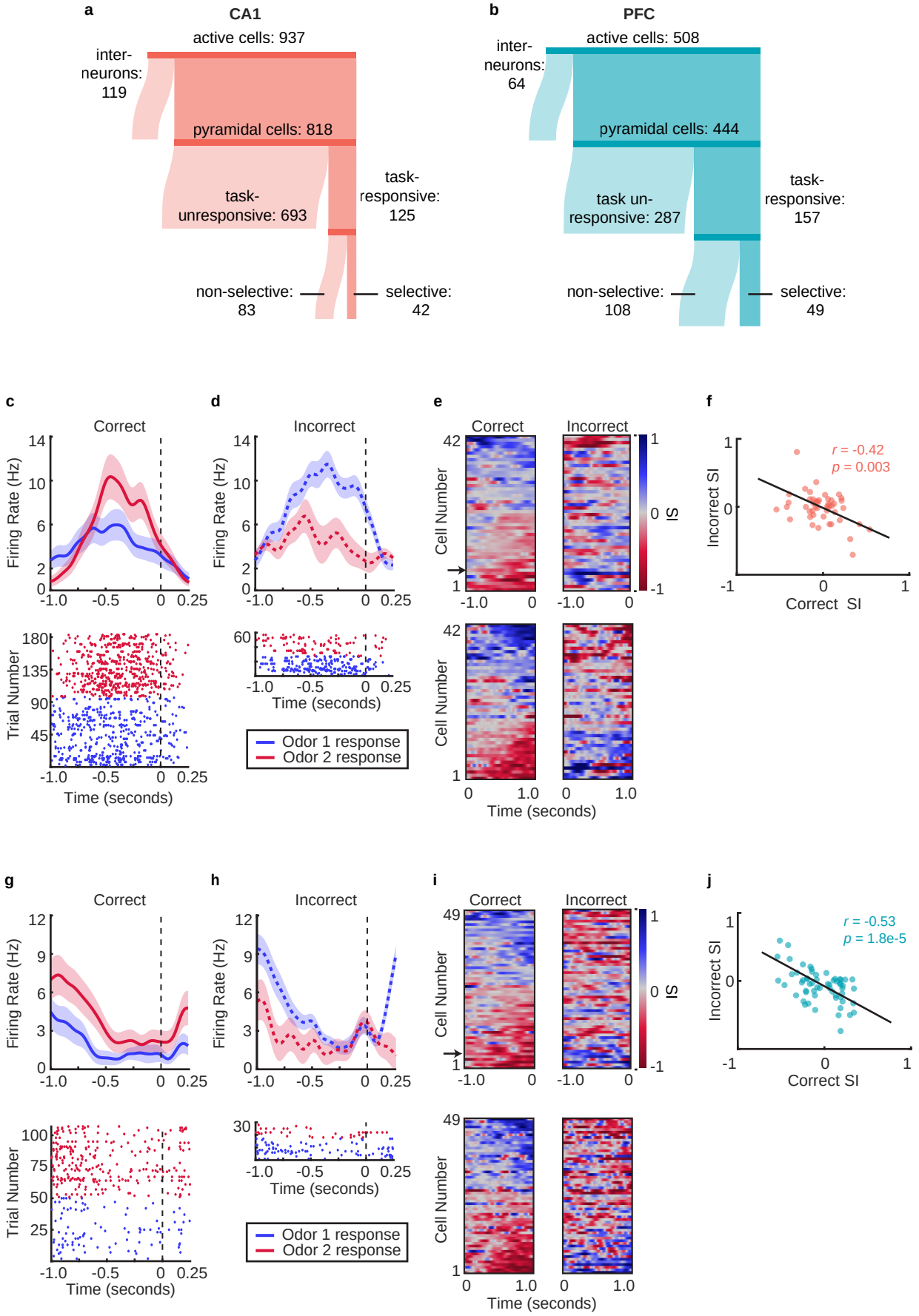
a
CA1
active cells: 937
inter-neurons: 119
pyramidal cells: 818
task-unresponsive: 693
task-responsive: 125
non-selective: 83
selective: 42
b
PFC
active cells: 508
inter-neurons: 64
pyramidal cells: 444
task un-responsive: 287
task-responsive: 157
non-selective: 108
selective: 49
c
Correct
Firing Rate (Hz)
Trial Number
Time (seconds)
d
Incorrect
Firing Rate (Hz)
Time (seconds)
Odor 1 response
Odor 2 response
e
Correct
Incorrect
Cell Number
SI
Time (seconds)
f
r = -0.42
p = 0.003
Incorrect SI
Correct SI
g
Correct
Firing Rate (Hz)
Trial Number
Time (seconds)
h
Incorrect
Firing Rate (Hz)
Time (seconds)
Odor 1 response
Odor 2 response
i
Correct
Incorrect
Cell Number
SI
Time (seconds)
j
r = -0.53
p = 1.8e-5
Incorrect SI
Correct SI

Figure 3: Single neurons in CA1 and PFC exhibit choice-selectivity during decision-making period

a. Sankey diagram showing the number of CA1 cells that were classified into different categories. Sizes of partitions are proportional to raw numbers.
b. Same as for a, but for PFC cells.
c. Example PSTH and raster plot for a single choice-selective CA1 neuron on correct trials, aligned to odor-port disengagement. Shaded areas indicate s.e.m. Firing rates are shown in Hz, referring to spikes/second.
d. Same as for c, but for Incorrect trials.
e. Selectivity index (SI) of all choice-selective cells in CA1 on correct trials (left) and incorrect trials (right), aligned to odor-port disengagement. SI is calculated as the difference in firing rate between Odor 1 trials and Odor 2 trials, divided by the sum of these firing rates. SI is color coded, where blue indicates an SI of 1 (absolute Choice 1 preference), red indicates an SI of -1 (absolute Choice 2 preference) and grey indicates an SI of 0 (not selective). Cells are sorted according to peak selectivity on correct trials and sorting order is the same for both plots.
f. Correlation between correct trial SI and incorrect trial SI for all choice-selective CA1 cells ($n = 42$, $r = -0.42$, $p = 0.003$**).

g-j. Same as a-e, but for PFC cells. Correlation in j: $n = 49$, $r = -0.53$, $p = 1.8e-5$***.

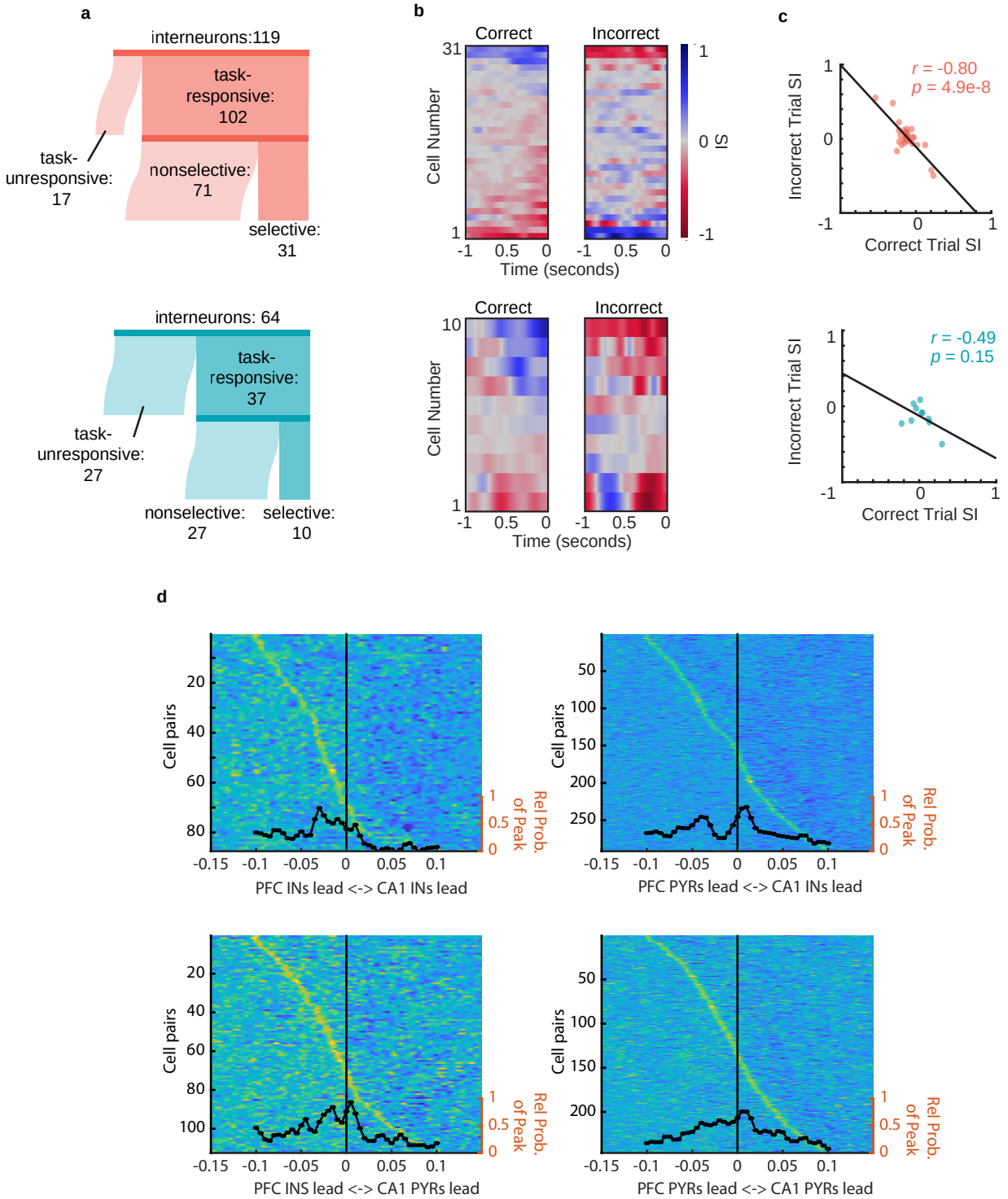
a
interneurons:119
task-responsive: 102
task-unresponsive: 17
nonselective: 71
selective: 31
interneurons: 64
task-responsive: 37
task-unresponsive: 27
nonselective: 27
selective: 10
b
Correct
Incorrect
Cell Number
Time (seconds)
SI
c
r = -0.80
p = 4.9e-8
r = -0.49
p = 0.15
Incorrect Trial SI
Correct Trial SI
d
Cell pairs
Rel Prob. of Peak
PFC INs lead <-> CA1 INs lead
PFC PYRs lead <-> CA1 INs lead
PFC INS lead <-> CA1 PYRs lead
PFC PYRs lead <-> CA1 PYRs lead

Figure 4: Interneurons exhibit choice-selectivity and temporal coordination during decision-making period

a. Sankey diagram showing the number of CA1 interneurons (top) and PFC interneurons (bottom) that were classified into different categories. Sizes of partitions are proportional to raw numbers.

b. Selectivity index (SI) of all choice-selective interneurons in CA1 (top) and PFC (bottom) on correct trials (left) and incorrect trials (right), aligned to odor-port disengagement.

c. Correlation between correct trial SI and incorrect trial SI for CA1 ($n = 31$, $r = -0.8$, $p = 4.9e-8$) and PFC ($n = 10$, $r = -0.49$, $p = 0.15$) interneurons.

d. Histograms and waterfall plots of significantly connected PFC-CA1 cell pairs. Peaks falling above zero indicate CA1 leading, whereas peaks falling below zero indicate PFC leading. One-sample Wilcoxson signed rank tests (H_0: $\mu = 0$ ms). Top-left: CA1-PFC interneuron pairs, $n = 87$ pairs, $p = 3.5e-8$; top-right: CA1 interneuron-PFC pyramidal pairs, $n = 283$ pairs, $p = 2.11e-3$; bottom-left: CA1 pyramidal-PFC interneuron pairs, $n = 111$ pairs, $p = 3.4e-3$, bottom right: CA1-PFC pyramidal pairs, $n = 224$ pairs, $p = 0.14$.

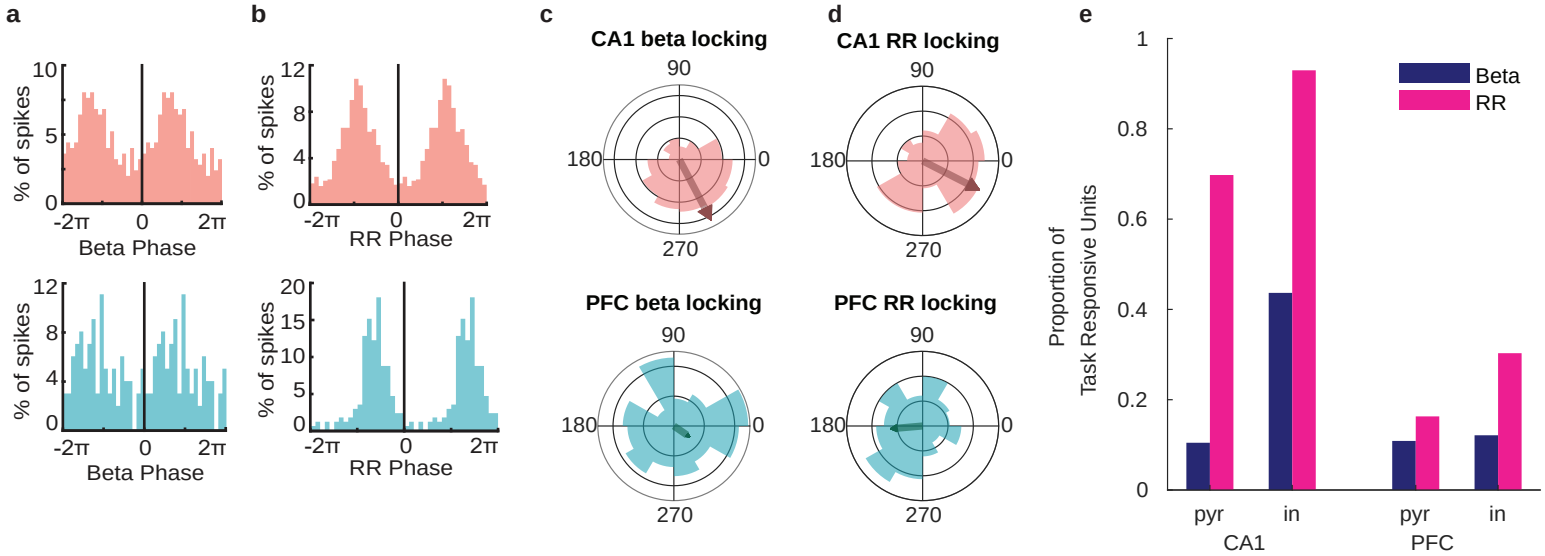
a
b
c
d
e
% of spikes
Beta Phase
RR Phase
CA1 beta locking
CA1 RR locking
PFC beta locking
PFC RR locking
90
180
0
270
Beta
RR
Proportion of Task Responsive Units
pyr
in
CA1
PFC

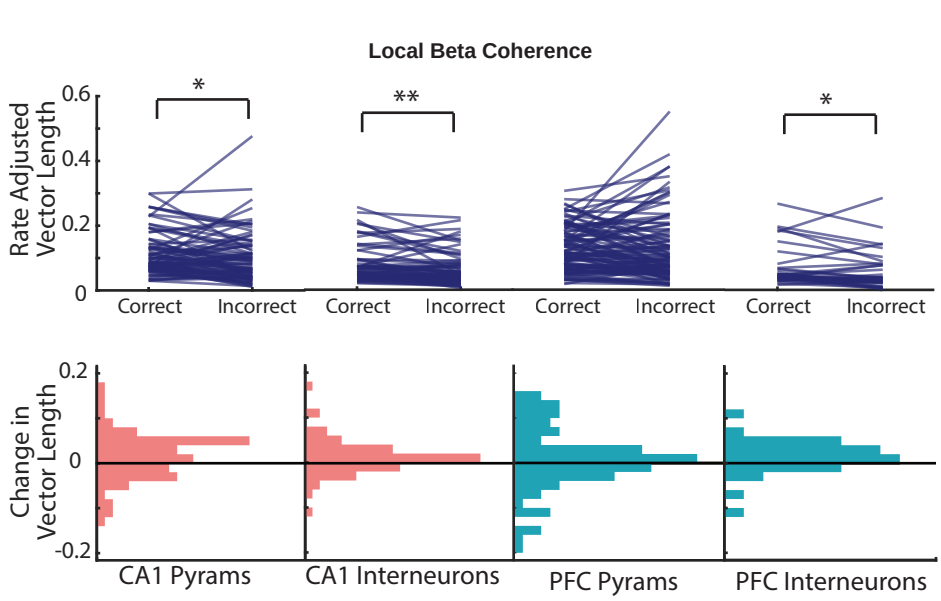
f
Local Beta Coherence
Rate Adjusted Vector Length
Correct
Incorrect
Change in Vector Length
CA1 Pyrams
CA1 Interneurons
PFC Pyrams
PFC Interneurons

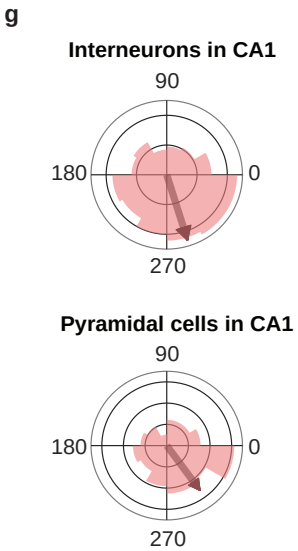
g
Interneurons in CA1
Pyramidal cells in CA1
90
180
0
270

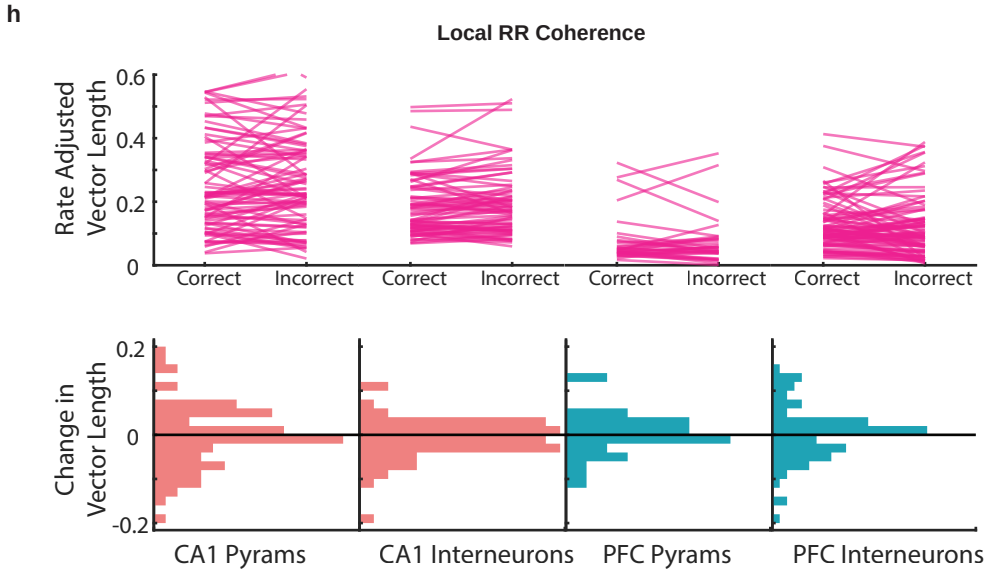
h
Local RR Coherence
Rate Adjusted Vector Length
Correct
Incorrect
Change in Vector Length
CA1 Pyrams
CA1 Interneurons
PFC Pyrams
PFC Interneurons

Figure 5: CA1 and PFC cells phase lock to beta and respiratory rhythms during decision making

a. Example spike-phase histograms from two example cells that are phase locked to the beta rhythm. Top: CA1 cell (Rayleigh Z test, n = 242 spikes, z = 15.5, p = 1.5e-7); bottom: PFC cell (n = 99 spikes, z = 4.86, p = 0.007). Phase axes are duplicated for visibility.

b. Example spike-phase histograms from two example cells that are phase locked to RR. Top: CA1 cell (Rayleigh Z test, n = 870 spikes, z = 135.3, p = 6.3e-62); bottom: PFC cell (n = 172 spikes, z = 73.9, p = 3.9e-37).

c. Polar histogram of preferred beta phases for all task-responsive CA1 (n = 157 cells, Rayleigh Z test, z = 12.22, p = 4.3e-6) and PFC (n = 125 cells, z = 0.36, p = 0.70) cells. Arrows indicate mean phase direction and magnitude.

d. Polar histogram of preferred RR phases for all task-responsive CA1 (Rayleigh Z test, z = 8.96, p = 2.01e-5) and PFC cells (z = 2.02, p = 0.13). Arrows indicate mean phase direction and magnitude.

e. Percentage of cells in CA1 and PFC that were phase locked to either beta or RR (Beta; CA1: pyr n = 12/86, 14.0%, in n= 29/71, 40.9%; PFC: pyr n = 6/92, 6.5%, in n = 4/33, 12.1%. RR; CA1: pyr n = 59/86, 68.6%, in n=66/71, 92.9%; PFC: pyr n = 15/92, 16.3%, in n=10/33, 30.3%).

f. Rate Adjusted Vector Length(top) and histogram of change in vector length from correct to incorrect trials(bottom) for all task-responsive cells in PFC and CA1 relative to local beta rhythm. (signed-rank tests, signed-rank tests, CA1: pyr n = 90, p = 0.019, in n=73, =p2.61e-3; PFC: pyr n = 98, p = 0.25, in n=33, p=0.043, *<.05, **<.01).

g. Polar histogram of preferred beta phases for all task responsive CA1 interneurons and pyramidal cells. (pyr n=86, p=2.81e-5, IN n=71, p=0.0179)

h. As in (f), but for all cells relative to local RR. (signed-rank tests, no test found significance below p=0.05).

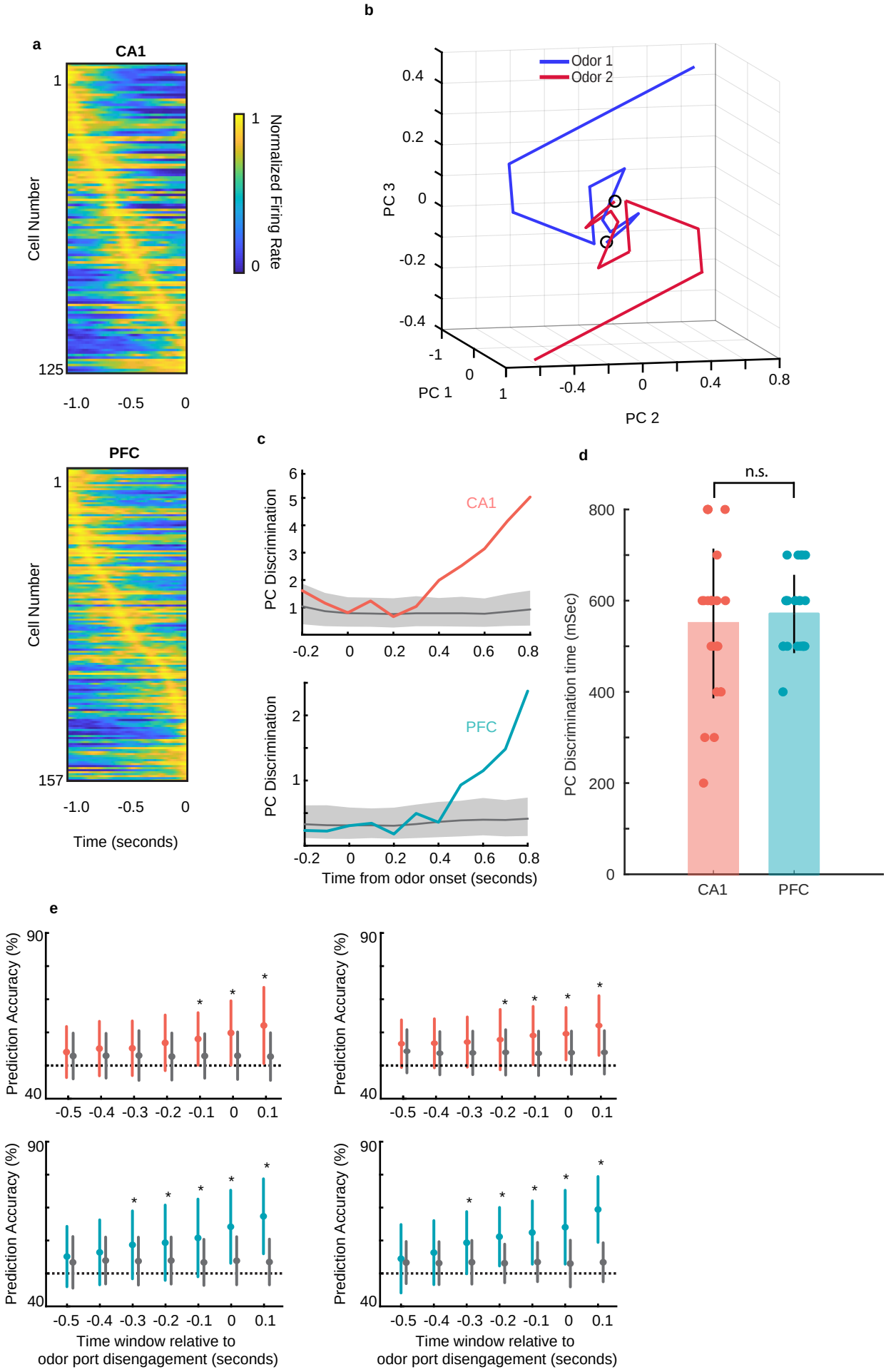
a
CA1
Cell Number
1
125
-1.0
-0.5
0
Normalized Firing Rate
1
0
PFC
157
Time (seconds)
b
Odor 1
Odor 2
PC 1
PC 2
PC 3
c
CA1
PFC
PC Discrimination
Time from odor onset (seconds)
d
n.s.
PC Discrimination time (mSec)
CA1
PFC
e
Prediction Accuracy (%)
Time window relative to
odor port disengagement (seconds)

Figure 6: Neural ensemble responses during decision making predict the upcoming choice

a. Normalized firing rate of all task-responsive cells in CA1 (top) and PFC (bottom) during a 1 second window before odor port disengagement.

b. Example session with average trajectories of CA1 population activity using the first three PC dimensions for the two choices (n = 43, 45 left-bound (blue) and right-bound (red) trials; n = 12 CA1 neurons in ensemble, 100 ms bins). The two trajectories showing a rapid evolution and separation within a few hundred ms after odor onset.

c. Euclidean distance between left-bound and right-bound average PC trajectories for an example CA1 ensemble (top, n = 12 neurons) and PFC ensemble (bottom, n = 10 neurons) was compared to a chance-level distance distribution computed by shuffling the odor identities across trials and creating a null distribution.

d. Neural discrimination times for CA1 and PFC locked to odor onset (n = 24 sessions CA1 range: 200-800 ms; PFC range, 400-700 ms) were similar (**Fig. 7c**; sign rank test, $p = 0.68$).

e. Neural discrimination times during odor sampling aligned to decision time. Colored error bars indicate real data mean ± s.d., whereas gray error bars indicate shuffled data mean ± s.d. Cells used for prediction include all task-responsive putative pyramidal cells in CA1 (top) and PFC (bottom) or all active neurons including interneurons (right). Stars indicate prediction time windows where the fraction of correctly predicted trials was significantly higher than the fraction from the shuffled data (rank-sum tests, * = $p < 0.05$).

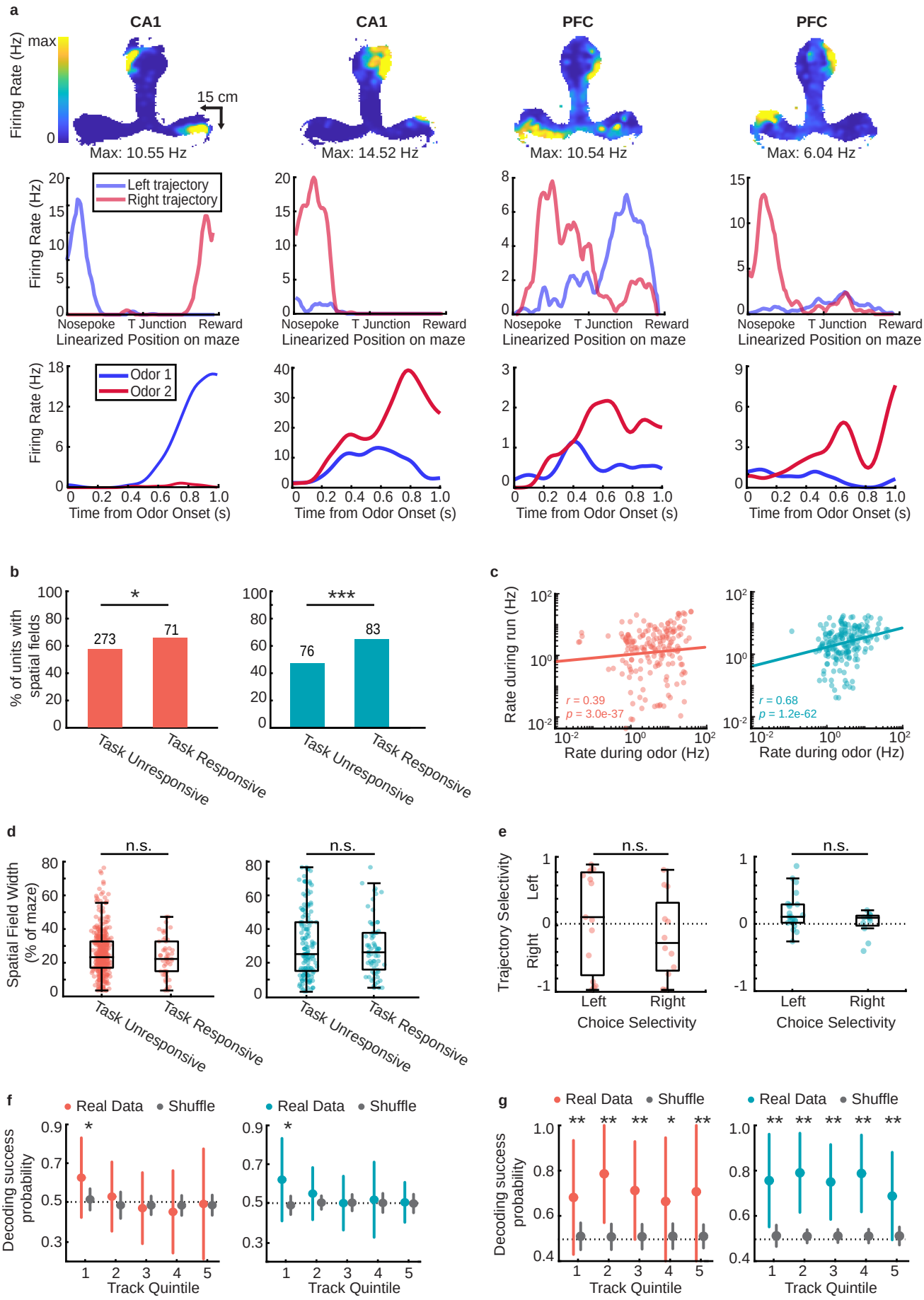
a
CA1
CA1
PFC
PFC
Firing Rate (Hz)
max
0
15 cm
Max: 10.55 Hz
Max: 14.52 Hz
Max: 10.54 Hz
Max: 6.04 Hz
Left trajectory
Right trajectory
Nosepoke
T Junction
Reward
Linearized Position on maze
Odor 1
Odor 2
Time from Odor Onset (s)
b
% of units with spatial fields
273
71
76
83
Task Unresponsive
Task Responsive
c
Rate during run (Hz)
Rate during odor (Hz)
r = 0.39
p = 3.0e-37
r = 0.68
p = 1.2e-62
d
Spatial Field Width (% of maze)
n.s.
e
Trajectory Selectivity
Left
Right
Choice Selectivity
f
Real Data
Shuffle
Decoding success probability
Track Quintile
g

Figure 7: Representations of choice and space are maintained independently during delay period

a. Example choice-selective units (CA1, first two columns, PFC, last two columns) with spatial fields on the track. Top row: Heat map illustrating spatial fields during run bouts. Middle row: Linearized spatial tuning curves for outbound left and right run trajectories. Bottom row: PSTHs showing odor responses during decision-making period (Odor selectivity indices, left to right: 0.92, -0.43, -0.40, -0.57).
b. Spatial field prevalence in task-unresponsive and task-responsive cells in CA1 (left) and PFC (right). CA1: 273/477 (57%) of task-unresponsive cells, and 71/108 (66%) of task-responsive cells had spatial fields (binomial test: $p = 0.03$*); PFC: 76/160 (48%) of task-unresponsive cells, and 83/128 (66%) of task-responsive cells had spatial fields (binomial test: $p = 2.7e-5$***).

c. Correlation between firing rates during run and firing rates during odor sampling period for all putative pyramidal cells in CA1 (left) and PFC (right). (CA1: $n = 585$ cells, $r = 0.39$, $p = 3.0e-37$; PFC: $n = 288$ cells, $r = 0.68$, $p = 1.2e-62$).
d. Spatial field width for odor unresponsive and odor responsive units in CA1 (left) and PFC (right). If a unit had a spatial field on both outbound trajectories, each field was counted separately. (Rank-sum tests; CA1: $n = 452$ fields, $p = 0.15$; PFC: $n = 207$ fields, $p = 0.92$).
e. Trajectory selectivity scores of choice-selective units according to preferred choice (Rank sum tests, CA1: $p = 0.26$; PFC: $p = 0.20$).
f. Decoding of choice identity by naïve Bayesian classifier according to CA1 (left) and PFC (right) task-responsive ensemble activity at five equally sized spatial quintiles along the full run trajectory of the maze. 1 spatial quintile = 24.6 cm (123 cm / 5). Colored error bars indicate real data mean ± s.d. whereas grey error bars indicate shuffled data mean ± s.d. Stars indicate quintiles where the fraction of correctly decoded trials was significantly higher than the fraction from the shuffled data (rank-sum tests, * = $p < 0.05$).
g. As in (f), but decoding of choice identity according to CA1 (left) and PFC (right) spatially-modulated ensemble activity at each spatial quintile. (rank-sum tests, * = $p < 0.05$, ** = $p < 0.01$).

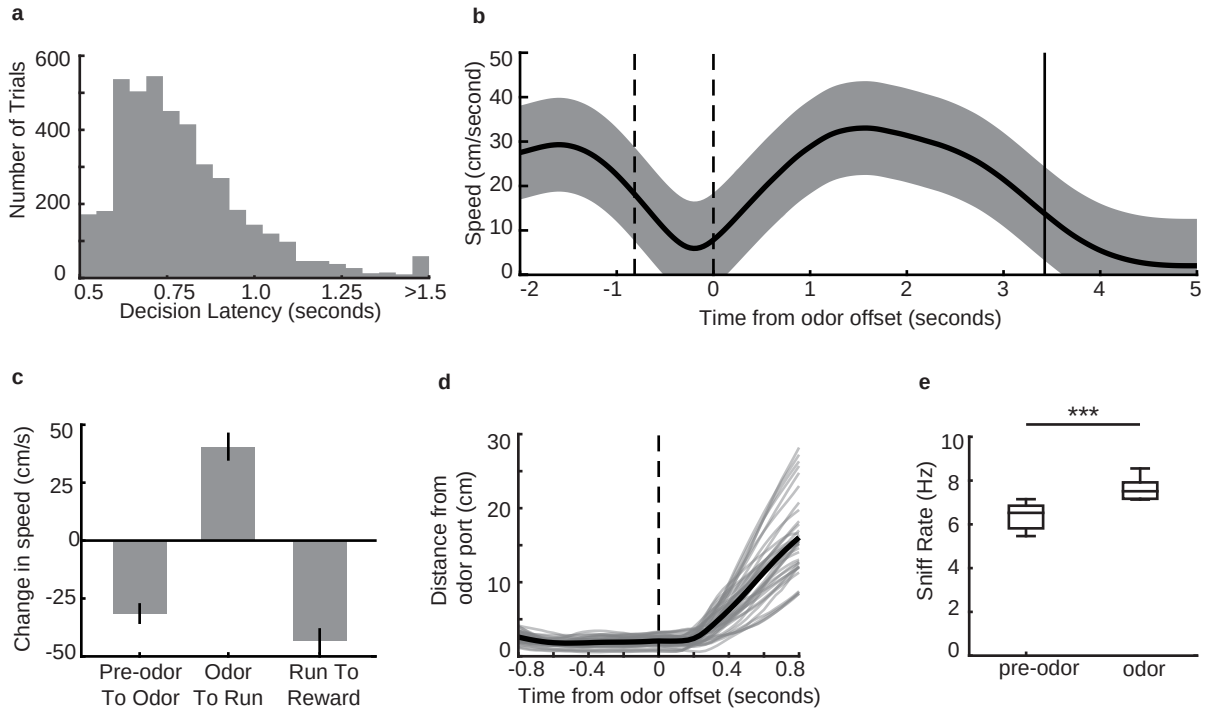
a
Number of Trials
600
400
200
0
0.5
0.75
1.0
1.25
>1.5
Decision Latency (seconds)
b
Speed (cm/second)
50
40
30
20
10
0
-2
-1
0
1
2
3
4
5
Time from odor offset (seconds)
c
Change in speed (cm/s)
50
25
0
-25
-50
Pre-odor To Odor
Odor To Run
Run To Reward
d
Distance from odor port (cm)
30
20
10
0
-0.8
-0.4
0
0.4
0.8
Time from odor offset (seconds)
e
***
Sniff Rate (Hz)
10
8
6
4
2
0
pre-odor
odor

Supplemental Figure 1 (Related to Figure 1). Behavioral parameters on the odor-place associative memory and decision-making task

a. Histogram of decision latencies. Mean: 0.82 seconds ± 0.25 s.d.
b. Mean run velocity across the full task for an example session from one animal, aligned to odor offset. Area between dashed lines indicates average odor-sampling period, solid line indicates average reward onset time. Shaded area indicates s.d.
c. Average change in speed across different task epochs, for all animals that ran on the full maze (and not the truncated maze) (n = 5). Error bars indicate s.d.
d. Distance from odor port over time aligned to odor port offset time. Grey lines are individual sessions, black line is mean across sessions. (n = 38 sessions).
e. Sniff rate as measured by the thermocouple signal, during odor (7.1 ± 0.39 Hz, mean ± s.e.m.) and time matched pre-odor periods (6.2 ± 0.29 Hz, mean ± s.e.m.). Box plots indicate interquartile ranges (signed-rank test, n = 11 sessions across 2 animals, p = 9.8e-4***).

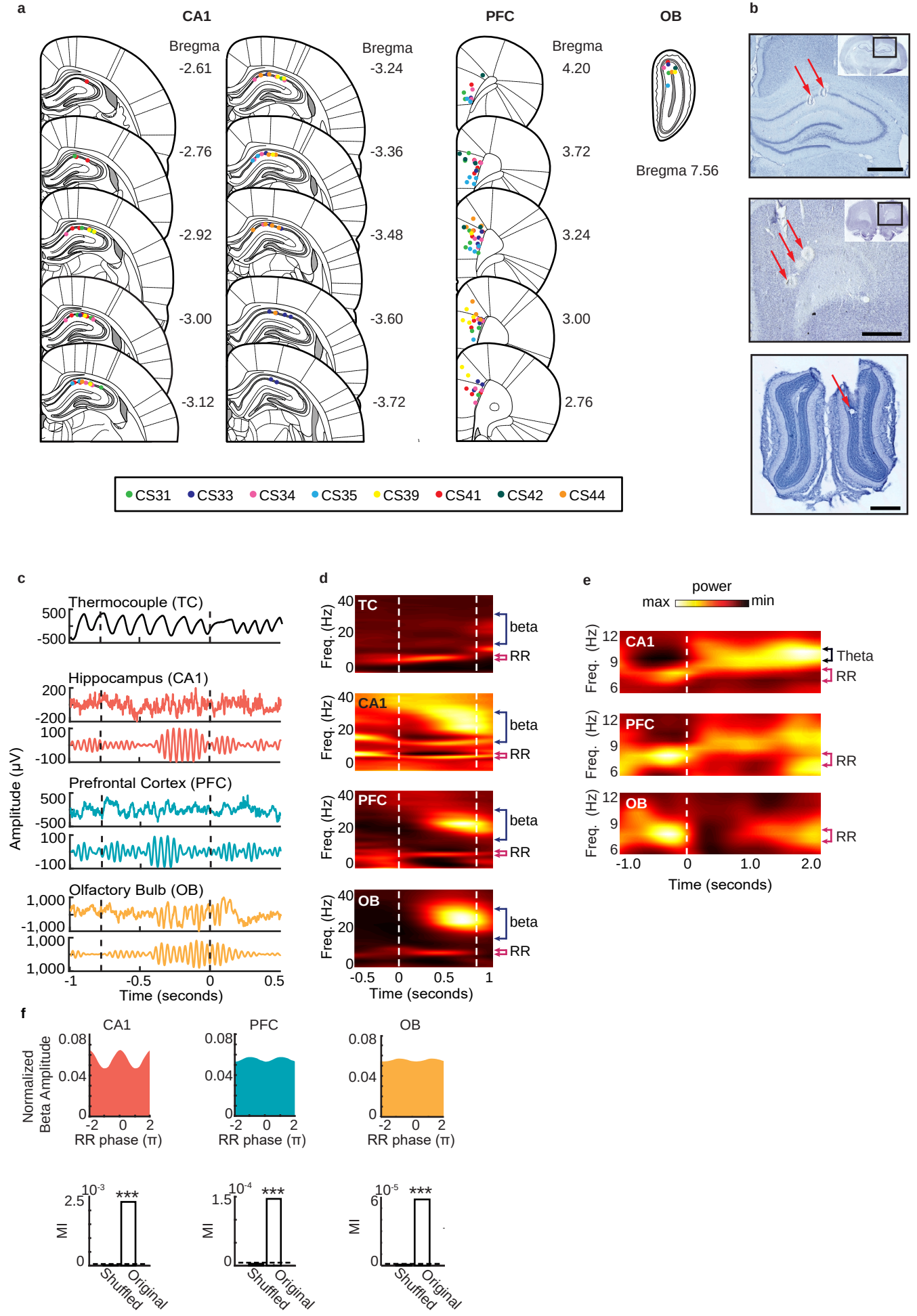
a
CA1
PFC
OB
Bregma
-2.61
-2.76
-2.92
-3.00
-3.12
Bregma
-3.24
-3.36
-3.48
-3.60
-3.72
Bregma
4.20
3.72
3.24
3.00
2.76
Bregma 7.56
CS31
CS33
CS34
CS35
CS39
CS41
CS42
CS44
b
c
Thermocouple (TC)
Hippocampus (CA1)
Prefrontal Cortex (PFC)
Olfactory Bulb (OB)
Amplitude (μV)
Time (seconds)
d
TC
CA1
PFC
OB
Freq. (Hz)
beta
RR
Time (seconds)
e
power
max
min
CA1
PFC
OB
Theta
RR
Freq. (Hz)
Time (seconds)
f
CA1
PFC
OB
Normalized Beta Amplitude
RR phase (π)
MI
***
Shuffled
Original

Supplemental Figure 2 (Related to Figure 2). Rhythmic activity in the olfactory-hippocampal-prefrontal network

a. Recording locations for 8 rats (color coded) where tetrode locations were recovered. The recording sites were reconstructed from the electrolytic lesions in *post hoc* Nissl-stained coronal brain sections and mapped onto the stereotaxic atlas[1]. Electrodes were localized to target areas in dorsal area CA1, medial prefrontal cortex (PFC), and granule cell layer of OB after histology (PFC electrodes localized primarily to prelimbic cortex, with a few electrodes in anterior cingulate cortex (ACC)).

b. Sample Nissl-stained brain sections showing final tetrode placement in hippocampus (top), PFC (middle), and olfactory bulb (bottom). Arrows indicate tetrode lesions. Scale bars each represent 1 mm.

c. Examples of thermocouple and LFP traces from one tetrode in each region during presentation of odor from one trial, aligned to odor port disengagement. Area between dashed lines indicates odor sampling period. Top to bottom: Respiratory rhythm recorded via thermocouple, CA1 signal, beta band (20-30 Hz) filtered CA1 signal, PFC signal, beta band filtered PFC signal, OB signal, beta band filtered OB signal.

d. Time-frequency plots showing power spectra across all animals aligned to odor onset (at time 0). Color scale represents z-scored power. Area between dashed lines indicates average odor sampling period. Beta band is marked by blue bracket, and RR band is marked by pink bracket. Thermocouple signal (TC), n = 12 sessions, max 0.92, min -0.30; CA1: n = 38 sessions, max 0.29, min -0.33; PFC: n = 38 sessions, max 0.58, min -0.15; and OB: n = 38 sessions, max 2.28, min -0.20.

e. Time-frequency spectrograms across animals that ran on the full maze, aligned to odor port disengagement (at time 0) and extending into the run period on the track. Color scale represents z-scored power for each region: CA1: max 0.45; min -0.34, PFC: max 0.21; min -0.14, and OB: max 0.72; min -0.16. Dashed line indicates odor port disengagement time. RR band is marked by pink bracket.

f. Phase-amplitude coupling between RR and beta, in CA1 (left), PFC (middle), and OB (right). Top row: normalized phase-amplitude histograms. Bottom row: modulation index (MI)[2] of real data compared to the MI from a trial-shuffled dataset (500 shuffles). Dashed line indicates significance level (alpha = 0.05, $p < 0.001$***).

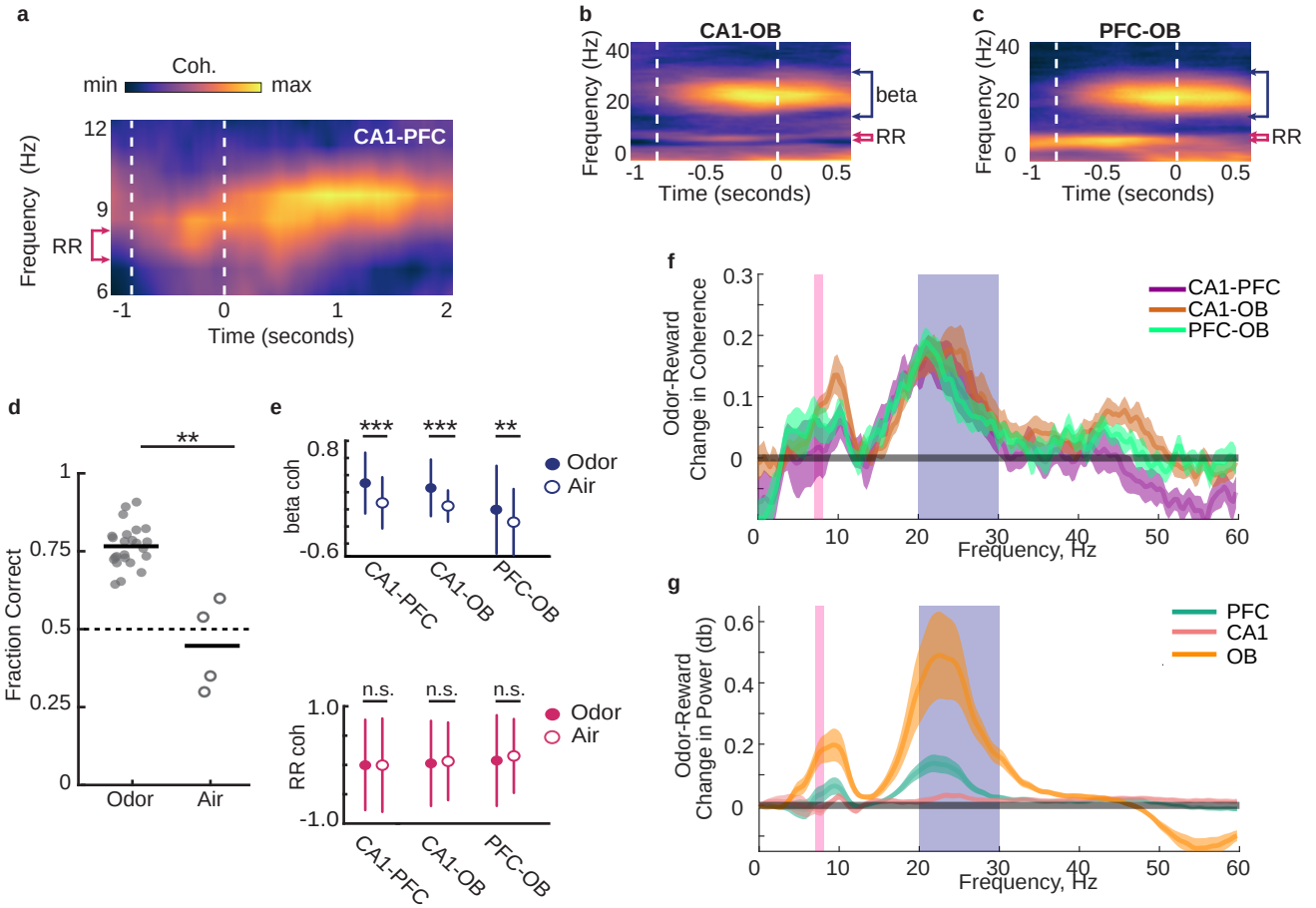
a
Coh.
min
max
CA1-PFC
Frequency (Hz)
12
9
6
RR
-1
0
1
2
Time (seconds)
b
CA1-OB
Frequency (Hz)
40
20
0
beta
RR
-1
-0.5
0
0.5
Time (seconds)
c
PFC-OB
Frequency (Hz)
40
20
0
RR
-1
-0.5
0
0.5
Time (seconds)
d
**
Fraction Correct
1
0.75
0.5
0.25
0
Odor
Air
e
***
***
**
beta coh
0.8
-0.6
Odor
Air
CA1-PFC
CA1-OB
PFC-OB
n.s.
n.s.
n.s.
RR coh
1.0
-1.0
Odor
Air
CA1-PFC
CA1-OB
PFC-OB
f
Odor-Reward
Change in Coherence
0.3
0.2
0.1
0
CA1-PFC
CA1-OB
PFC-OB
0
10
20
30
40
50
60
Frequency, Hz
g
Odor-Reward
Change in Power (db)
0.6
0.4
0.2
0
PFC
CA1
OB
0
10
20
30
40
50
60
Frequency, Hz

Supplemental Figure 3 (Related to Figure 2). Beta coordination underlies decision making based on odor-place associations

a. CA1-PFC coherence across animals that ran on the full maze, aligned to odor port disengagement and extending into the run period on the track. Color scale represents z-scored coherence. Min = -0.18, max = 0.50. Dashed line indicates odor port disengagement time. RR band is marked by pink bracket.

b. Top: CA1-OB coherence spectra across all animals and all tetrode pairs (n = 38 sessions). Area between vertical dashed lines indicates mean decision-making period, aligned to odor port disengagement. Color scale represents z-scored coherence (max 0.41, min -0.25). Middle: Beta (15-30 Hz) coherence during odor periods and time-matched pre-odor periods. (signed-rank test, n = 38 sessions, p = 1.7e-7***). Bottom: RR (7-8 Hz) coherence during odor periods and time-matched pre-odor periods. (signed-rank test, p = 6.3e-4***).

c. As in (b), but for PFC-OB coherence. Top: max 0.45, min -0.28. Middle: signed-rank test, p = 4.3e-7. Bottom: signed-rank test, p = 0.30.

d. Performance of three animals on the odor-cued task (n = 24 sessions) versus the air-cued task (n = 4 sessions) in which animals were presented with only air as a neutral stimulus instead of two distinct odors. Black bars indicate mean. Dashed line indicates chance level. (Rank-sum test, p = 0.002**)

e. Beta (top row) and RR (bottom row) Z-scored coherence between CA1-PFC, CA1-OB and PFC-OB on correct trials with odors (n = 3174) and randomly rewarded trials with only air presented at the odor port (n = 134). Correct trials were randomly subsampled with replacement to match the number of incorrect trials 1000 times. Error bars indicate s.d. of real data distributions. (Bootstrap tests: beta: CA1-PFC: p < 0.001***, CA1-OB, p < 0.001***, PFC-OB: p = 0.002**; RR: CA1-PFC: p = 0.49, CA1-OB, p = 0.30, PFC-OB, p = 0.12)

f. Change in coherence from reward period to odor period. Beta coherence during odor sampling was higher for all pairs (sign rank test; CA1-PFC p-0.01, CA1-OB 0=0.0012, PFC-OB p=0.0024) and RR coherence was higher only for OB-CA1 and OB-PFC (CA1-PFC p=0.56, CA1-OB p=0.0044, PFC-OB p=0.64e-4)

g. Change in power from reward period to odor period. Beta power increased in all three regions from reward to odor sampling (sign rank test, CA1 p=0.0012, PFC p=5.3e-4, OB p=4.4e-4) whereas RR power only increased in OB (CA1 p=0.062, PFC p=0.11, OB p=4.4e-4)

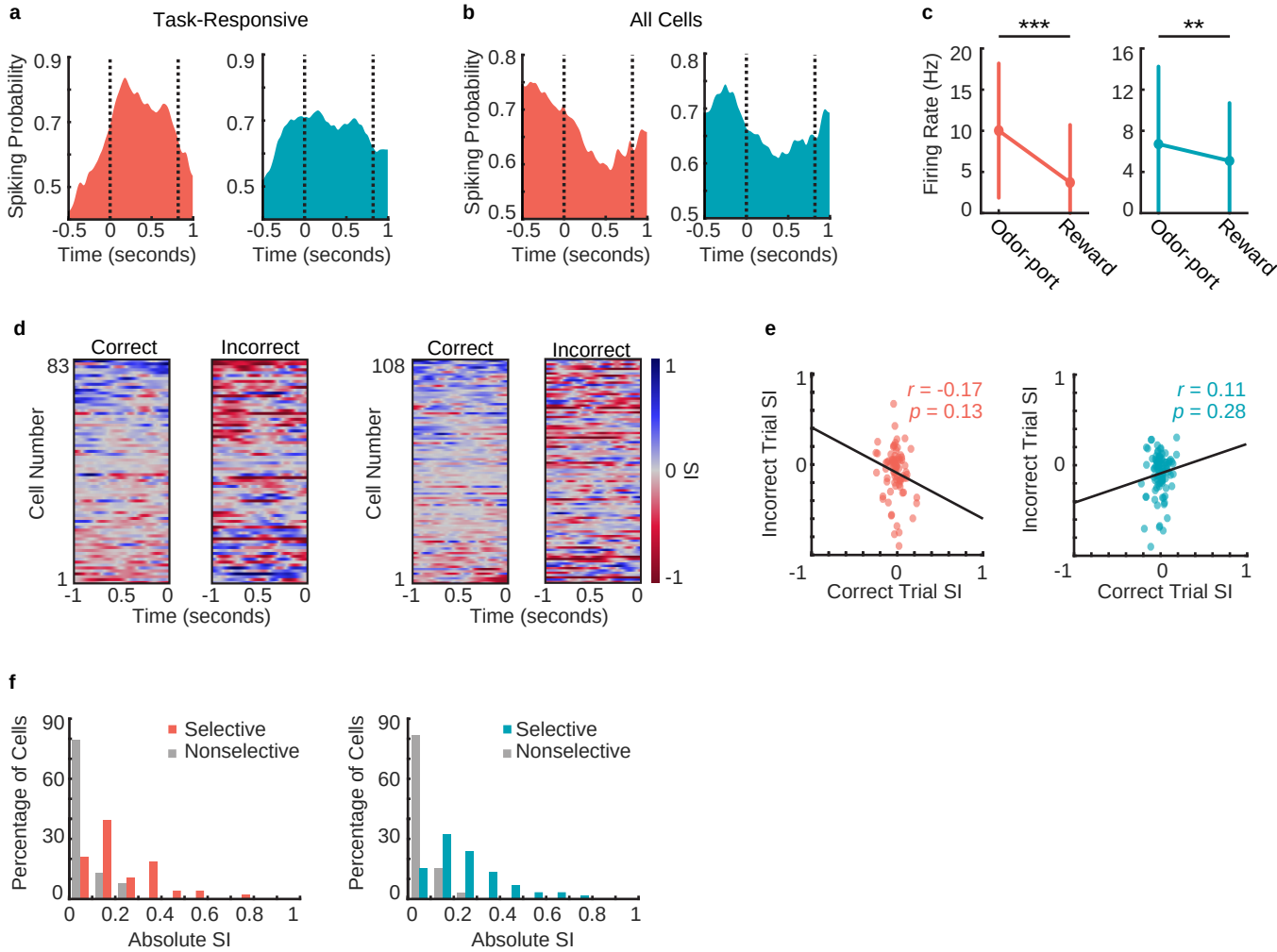
a
Task-Responsive
Spiking Probability
Time (seconds)
b
All Cells
Spiking Probability
Time (seconds)
c
***
**
Firing Rate (Hz)
Odor-port
Reward
d
Correct
Incorrect
Cell Number
Time (seconds)
SI
e
r = -0.17
p = 0.13
r = 0.11
p = 0.28
Incorrect Trial SI
Correct Trial SI
f
Selective
Nonselective
Percentage of Cells
Absolute SI

Supplemental Figure 4 (Related to Figures 3 and 4). Neural responses during decision-making period

a. Spiking probability during decision-making period for all task-responsive cells in CA1 (left, n = 125 cells) and PFC (right, n = 157 cells). Area between the dashed lines represents decision-making period.
b. Spiking probability during decision-making period for all cells (task-responsive and task unresponsive, putative pyramidal cells and interneurons combined) in CA1 (left, n = 917 cells) and PFC (right, n = 507 cells). Area between the dashed lines represents decision-making period.
c. Firing rates of task-responsive pyramidal neurons during odor sampling and reward consumption (Signed-rank tests. CA1 (left): n = 125 cells, p = 5.1e-13; PFC (right): n = 157 cells, p = 0.009).
d. Selectivity index (SI) of all task-responsive but not choice-selective pyramidal cells in CA1 (left 2 panels) and PFC (right 2 panels) on correct trials and incorrect trials, aligned to odor port disengagement. Cells are sorted according to peak selectivity on correct trials and sorting order is the same for both plots.
e. Correlation between correct trial SI and incorrect trial SI for all non-choice-selective pyramidal neurons. (CA1 (left): n = 83 cells, r = -0.34, p = 0.001**; PFC (right): n = 108 cells, r = -0.34, p = 3.0e-4***).
f. Histograms showing absolute selectivity indices for choice selective vs. non-choice-selective pyramidal cell populations in CA1 (left) and PFC (right).

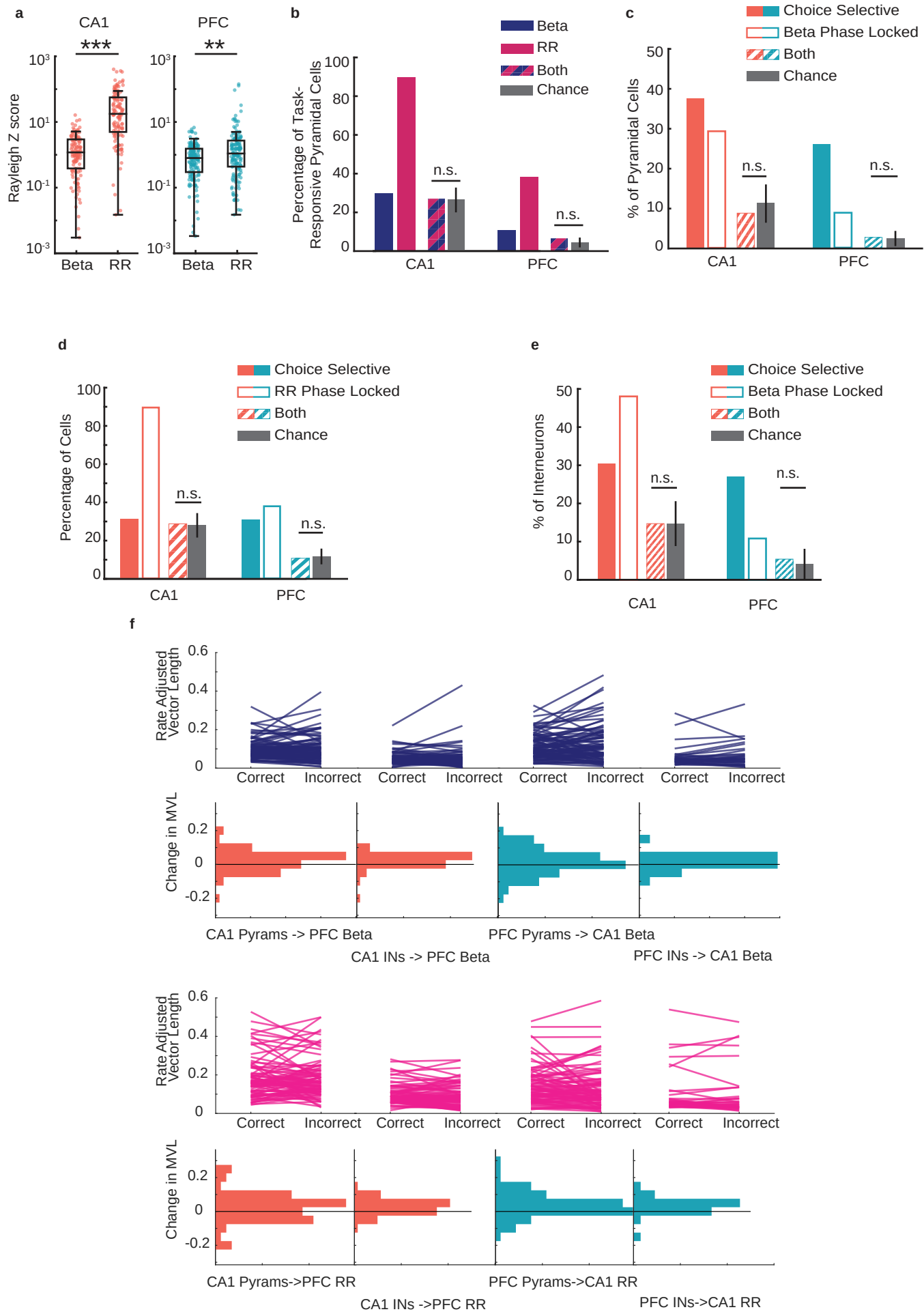
a
CA1
PFC
***
**
Rayleigh Z score
Beta
RR
b
Beta
RR
Both
Chance
Percentage of Task-Responsive Pyramidal Cells
n.s.
CA1
PFC
c
Choice Selective
Beta Phase Locked
Both
Chance
% of Pyramidal Cells
d
Choice Selective
RR Phase Locked
Both
Chance
Percentage of Cells
e
Choice Selective
Beta Phase Locked
Both
Chance
% of Interneurons
f
Rate Adjusted Vector Length
Correct
Incorrect
Change in MVL
CA1 Pyrams -> PFC Beta
CA1 INs -> PFC Beta
PFC Pyrams -> CA1 Beta
PFC INs -> CA1 Beta
CA1 Pyrams->PFC RR
CA1 INs ->PFC RR
PFC Pyrams->CA1 RR
PFC INs->CA1 RR

Supplemental Figure 5 (Related to Figure 5). Phase locking to respiratory rhythm

a. Rayleigh Z scores for spike-phases of task-responsive cells for beta and RR (rank-sum test; CA1: n = 125 cells, p = 3.2e-26***; PFC: n = 157 cells, p = 0.002**).

b. Percentage of task-responsive pyramidal cells in CA1 and PFC that were phase locked to beta, RR, or both beta and RR. Grey bars indicate chance level of cells being phase locked to both rhythms, error bars indicate the range of cell percentages that fall within the 95% bounds of the chance binomial distribution. Binomial tests. CA1: p = 0.08; PFC: p = 0.06.

c. Percentage of cells that are choice-selective (solid bars), phase-locked to the beta rhythm (outlined bars), and both choice-selective and phase-locked (striped bars). Grey bars indicate chance level of cells being both choice-selective and phase-locked, error bars indicate the range of cell percentages that fall within the 95% bounds of the chance binomial distribution. (binomial test, CA1: p = 0.08; PFC: p = 0.16).

d. Percentage of cells that are choice-selective (solid bars), phase-locked to RR (outlined bars), and both choice-selective and phase-locked (striped bars). Grey bars indicate chance level of cells being both choice-selective and phase-locked, error bars indicate the range of cell percentages that fall within the 95% bounds of the chance binomial distribution (Binomial test, CA1: p = 0.077; PFC: p = 0.10).

e. As in (c), but for interneurons. (binomial test; CA1: p = 0.11; PFC: p = 0.20)

f. Rate adjusted vector length (top) and histogram of change in vector length from correct to incorrect trials (bottom) for all task responsive neurons in PFC and CA1 relative to cross-region Beta and RR. No comparisons revealed significant results. (signed-rank tests, all p>.05)

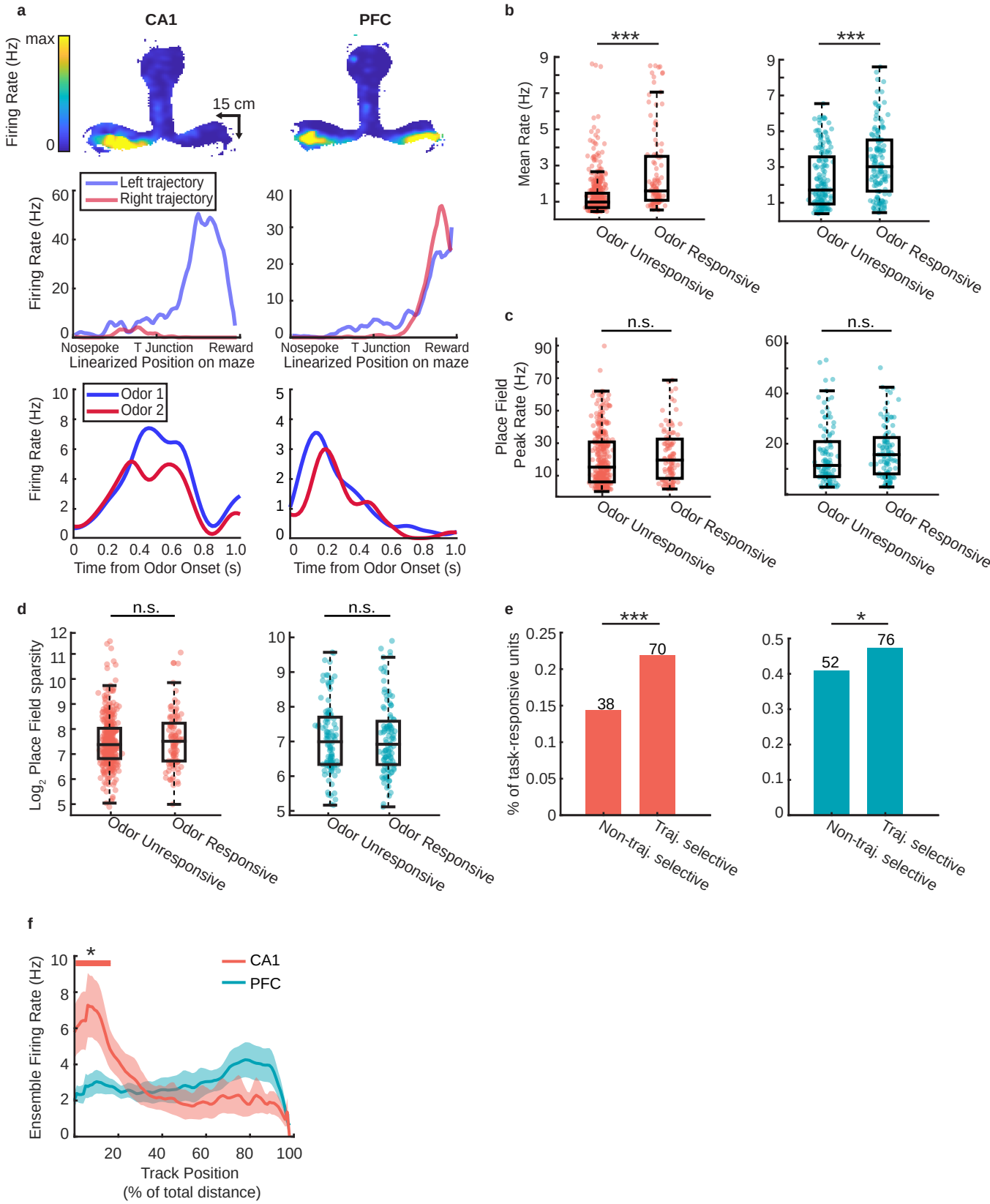
a
CA1
PFC
max
0
Firing Rate (Hz)
15 cm
Left trajectory
Right trajectory
Firing Rate (Hz)
Nosepoke
T Junction
Reward
Linearized Position on maze
Odor 1
Odor 2
Time from Odor Onset (s)
b
***
Mean Rate (Hz)
Odor Unresponsive
Odor Responsive
c
n.s.
Place Field Peak Rate (Hz)
d
Log2 Place Field sparsity
e
% of task-responsive units
38
70
52
76
Non-traj. selective
Traj. selective
f
CA1
PFC
Ensemble Firing Rate (Hz)
Track Position
(% of total distance)

Supplemental Figure 6 (Related to Figure 7). Spatial activity of task-responsive and task-unresponsive neurons.

a. Example task-responsive (but not choice-selective) units from CA1 (left) and PFC (right) with spatial fields on the track. Top row: Heat map of firing fields during run bouts. Middle row: Linearized spatial tuning curves for outbound left and right run trajectories. Bottom row: PSTHs showing odor responses during decision-making period.
b. Mean firing rate of task-responsive and task-unresponsive units during running on the maze, excluding decision-making periods (Rank-sum tests: CA1 (left): n = 585 cells, p = 2.8e-14***; PFC (right): n = 288 cells, p = 1.3e-5***).
c. Place field peak rate for task-responsive and task-unresponsive cells. (Rank sum tests, CA1 (left): n = 452 fields, p = 0.14; PFC (right): n = 207 fields, p = 0.08).
d. Place field sparsity for task-responsive and task-unresponsive cells. (Rank sum tests, CA1 (left): p = 0.70; PFC (right): p = 0.88).
e. Percentage of trajectory selective and non-trajectory selective cells that that were also task-responsive (Binomial tests: CA1 (left): n = 108 odor responsive units, p = 3.0e-4***; PFC (right): n = 128 odor responsive units, p = 0.02*).
f. Mean ensemble firing rate of task-responsive units in CA1 and PFC during outbound runs. Solid line indicates mean, shaded area represents s.d. Thick colored bar above marks positions in which the ensemble rate exceeds the 99th percentile of a bootstrap randomized null mean ensemble rate.

REFERENCES

1 Paxinos, G. & Watson, C. *The Rat Brain in Stereotaxic Coordinates*. (Academic Press, 2004).

2 Tort, A. B., Komorowski, R., Eichenbaum, H. & Kopell, N. Measuring phase-amplitude coupling between neuronal oscillations of different frequencies. *J Neurophysiol* **104**, 1195-1210, doi:jn.00106.2010 [pii]10.1152/jn.00106.2010 (2010).